Gravity Wave Diagnosis Using Empirical Normal Modes

MARTIN CHARRON*

Department of Atmospheric and Oceanic Sciences, McGill University, Montreal, Quebec, Canada

GILBERT BRUNET

Recherche en Prévision Numérique, Service de l'Environnement Atmosphérique, Dorval, Quebec, Canada

(Manuscript received 16 September 1997, in final form 12 November 1998)

ABSTRACT

The theory of empirical normal modes (ENMs) is adapted to diagnose gravity waves generated by a relatively high-resolution numerical model solving the primitive equations. The ENM approach is based on the principal component analysis (which consists of finding the most efficient basis explaining the variance of a time series), except that it takes advantage of wave-activity conservation laws. In the present work, the small-amplitude version of the pseudoenergy is used to extract from data quasi-monochromatic three-dimensional empirical modes that describe atmospheric wave activity. The spatial distributions of these quasi-monochromatic modes are identical to the normal modes of the linearized primitive equations when the underlying dynamics can be described with a stochastic linear and forced model, thus establishing a bridge between statistics and dynamics. This diagnostic method is used to study inertia–gravity wave generation, propagation, transience, and breaking over the Rockies, the North Pacific, and Central America in the troposphere–stratosphere–mesosphere Geophysical Fluid Dynamics Laboratory SKYHI general circulation model at a resolution of 1° of latitude by 1.2° of longitude. Besides the action of mountains in exciting orographic waves, inertia–gravity wave activity has been found to be generated at the jet stream level as a possible consequence of a sustained nonlinear and ageostrophic flow. In the tropical region of the model (Central America), the inertia–gravity wave source mechanism produced mainly waves with a westward vertical tilt. A significant proportion of these inertia–gravity waves was able to reach the model mesosphere without much dissipation and absorption.

1. Introduction

The large amount of atmospheric data now available, either obtained from measurements or model produced, often brings the need for compression of information. If one is interested in diagnosing phenomena with length scale or timescale of a given order from a large dataset, one might need to reduce the number of degrees of freedom associated with the time series. But in doing so, the dynamical character of the phenomenon under study should be preserved as much as possible. In a fully developed nonlinear or turbulent system, this task is one of great difficulty (there may even be no acceptable solution to this problem), and we will not address this question here. For a system that is linear, unforced, and free of noise, a simple Fourier analysis might be sufficient to extract modes that are dynamically significant. In the case of the atmosphere, linear and nonlinear regimes coexist. For example, planetary-scale normal modes have been found to propagate in the stratosphere (e.g., the ''5-day wave''; Hirota and Hirooka 1984). Methods that can extract statistical modes or space–time coherent structures from any kind of fields (linear or nonlinear) have been extensively discussed in the literature. For example, principal component analysis (PCA) (see Preisendorfer 1988; Sirovitch and Everson 1992; among others) is very efficient in reducing the number of degrees of freedom needed to represent a given time series. But the statistical modes obtained using the PCA technique may not bear any dynamical meaning at all.

Ideally, one would like to expand fields using the most suitable basis. A good choice when dealing with dynamical systems would be a coherent spatiotemporal basis for which each member is in dynamical balance, for example, a solution of the evolution equation. Of course, such a basis is impossible to find when the dynamical system is fully nonlinear, but when the dynamics is weakly nonlinear, it can approximated by

* Current affiliation: Centre National de Recherches Météorologiques, Météo-France, CNRM/GMAP, Toulouse, France.

Corresponding author address: Dr. Gilbert Brunet, Recherche en Prévision Numérique, 2121 route Trans-canadienne, Dorval, PQ H9P 1J3, Canada.
E-mail: gilbert.brunet@ec.gc.ca

taking into account appropriate conservation laws (Brunet 1994). The approach taken by Brunet was to find the eigenvectors of a matrix formed by the product of a covariance matrix and the matrix defining the bilinear form of a wave activity. If this basis is to be truly relevant, then it should be observed in its dynamical behavior. Brunet and Vautard (1996) have shown that the predictive skill of empirical normal modes (ENMs) is, in general, greater than that of standard empirical orthogonal functions (EOFs) for a shallow water atmosphere that is stochastically forced. Also, they have shown that the predictive skill and the linear dynamical interpretation of the ENMs are robust to weak nonlinear effects in a series of wave-breaking experiments.

The purpose of this study is to propose a general method suitable for all latitudes that can assess quantitatively the importance of each dynamical mode (defined to be in near-dynamical balance), focusing on gravity waves. A well-known method used to isolate inertia–gravity wave modes at midlatitudes in numerical models is to take the horizontal divergence of the velocity field. By doing so, one can filter out quasigeostrophic modes but cannot isolate monochromatic gravity waves. The cospectral method (Hayashi 1982) is another approach that gives an overall picture of the wave field at a given latitude and height but cannot isolate dynamical modes. In this work, the empirical normal mode formalism will be applied on an atmospheric model–generated dataset to extract and study gravity wave modes.

Section 2 deals with the formulation and physical interpretation of the empirical normal mode diagnostic tool with the presence of stochastic forcing in the dynamical system. We will argue that this permits a direct extraction of the normal mode spatial distribution from a linear stochastically forced time series, which is not possible with a standard time spectral analysis. In section 3, we identify the geographical locations analyzed by the method explained in section 2. Then results obtained from a general circulation model [Geophysical Fluid Dynamics Laboratory (GFDL) SKYHI] will be presented in section 4.

2. Theory of empirical normal modes

A diagnostic tool developed by Brunet (1994) that uses conservation of wave activity will be presented and adapted for the purpose of gravity wave diagnosis. This method allows one to statistically extract the normal modes of a linear dynamical system. At the end of this section, we will extend this idea to stochastically forced processes.

In general, a dynamical system can be written as

$$\frac{\partial \mathbf{f}}{\partial t} = \mathbf{G}(\mathbf{f}),$$

where $\mathbf{G}$ can be a nonlinear operator.

If the system is linearized about a time-independent basic state $\mathbf{f}_0$ [where $f(\mathbf{x}, t) = \mathbf{f}_0(\mathbf{x}) + \mathbf{f}'(\mathbf{x}, t)$] which is a solution of $\mathbf{G}(\mathbf{f}_0) = 0$, and if the linearized evolution equation is

$$\frac{\partial \mathbf{f}'}{\partial t} = i\mathbf{HBf}', \tag{2.1}$$

where $\mathbf{B}$ and $\mathbf{H}$ are time-independent Hermitian operators and $\mathbf{f}'$ is assumed to be a complex vector, it is then easily seen that a conserved quantity of the form $(\mathbf{f}', \mathbf{Bf}')$ is generated. The notation $(\mathbf{f}, \mathbf{g}) = \int d\mathbf{x}\, \mathbf{f}^{\dagger}\mathbf{g}$ is used. The converse is true: if $\mathbf{B}$ is nonsingular, we can always write Eq. (2.1) if $(\mathbf{f}', \mathbf{Bf}')$ is conserved. In fact, $(\mathbf{f}', \mathbf{Bf}')$ is an integrated wave activity. There are as many quadratic globally conserved quantities as there are nontrivial ways of rewriting $\mathbf{HB}$, keeping each term Hermitian. Hence, if $\mathbf{HB}$ equals $\mathbf{H}'\mathbf{B}'$, where $\mathbf{H}'$ and $\mathbf{B}'$ are Hermitian, then $(\mathbf{f}', \mathbf{B}'\mathbf{f}')$ will also be globally conserved [here $(\mathbf{f}', \mathbf{B}'\mathbf{f}')$ may be the pseudomomentum, and $(\mathbf{f}', \mathbf{Bf}')$ the pseudoenergy]. The evolution equation for $\mathbf{f}'$ in Eq. (2.1) is written as the product of two distinct Hermitian operators ($\mathbf{H}$ and $\mathbf{B}$) since the linearized primitive equations describing atmospheric motions can be put into this generalized Hermitian form [the fact that conserved small-amplitude wave activities exist confirms that Eq. (2.1) is the correct generic form]. An explicit description of $\mathbf{H}$ is given in Brunet and Vautard (1996) for the case of the shallow water equations. A normal mode $\mathbf{f}'_n$ will be a solution of Eq. (2.1) with a single frequency of oscillation ω_n:

$$\omega_n \mathbf{f}'_n = \mathbf{HBf}'_n. \tag{2.2}$$

The implication is that as long as $\mathbf{B}$ is nonsingular, ω_n will be real and the normal modes will be stable. Unstable modes can arise only when $\mathbf{B}$ is singular. Following Held (1985), two normal modes are orthogonal under the bilinear form defined by $\mathbf{B}$. Hence, $(\mathbf{f}'_m, \mathbf{Bf}'_n) = \lambda_n \delta_{mn}$, where λ_n is not necessarily positive since $\mathbf{B}$ may not be sign definite.

The basic idea of the empirical normal mode formulation is to take advantage of the orthogonality relationship in the definition of a modified EOF methodology. If the EOF covariance matrix is replaced by

$$\mathbf{K}(\mathbf{x}, \mathbf{y}) = \frac{1}{2T}\int_{-T}^{T} dt\mathbf{f}'(\mathbf{x}, t) \times \mathbf{f}'^{\dagger}(\mathbf{y}, t)\mathbf{B}(\mathbf{y}) \equiv \mathbf{C}(\mathbf{x}, \mathbf{y})\mathbf{B}(\mathbf{y}), \tag{2.3}$$

then its eigenvectors $\mathbf{f}'_n$, where

$$\int_V d\mathbf{y}\mathbf{K}(\mathbf{x}, \mathbf{y})\mathbf{f}'_n(\mathbf{y}) = \lambda_n \mathbf{f}'_n(\mathbf{x}), \tag{2.4}$$

are the normal modes. The expansion $\mathbf{f}'(\mathbf{x}, t) = \Sigma\, a_n(t)\mathbf{f}'_n(\mathbf{x})$ and $(1/2T)\int_{-T}^{T} a_m a_n^*\, dt = \delta_{mn}$ (in the limit $T \to \infty$) have been used. The time series is defined on the time interval $[-T, T]$ and we assume that all modes have been excited initially. Note that this time series

could be replaced by an ensemble of independent realizations that span all the possible excitations of normal modes without changing the results that follow. The summation in the expansion must be replaced by an integral when dealing with a continuous spectrum. But in practice, the fields are discretized, and the integrals are replaced by summations that simplify the problem of the singular mode continuous spectrum. We will then, in general, consider the operator $\mathbf{G}$ to operate from R_N to R_N where N is finite and is the dimension of the space used to represent the dataset.

Another simple way to interpret Eq. (2.4) is to note that the operators $\mathbf{HB}$ and $\mathbf{K} \equiv \mathbf{CB}$ commute ($\mathbf{HBCB} - \mathbf{CBHB} = 0$) and thus have the same set of eigenvectors (the normal modes) if they are nondegenerate operators. The above commutation relation is simply obtained by multiplying Eq. (2.1) by $\mathbf{f}'^{\dagger}$ on the right, and taking the time average (denoted by $\langle \cdot \rangle$):

$$\left\langle \frac{\partial \mathbf{f}'}{\partial t} \mathbf{f}'^{\dagger} \right\rangle = i\mathbf{HBC}. \tag{2.5}$$

Integrating by parts, the left-hand side of Eq. (2.5) can also be written $-\langle \mathbf{f}' \partial \mathbf{f}'^{\dagger}/\partial t \rangle = i\mathbf{CBH}$. This equality is obtained by taking the complex conjugate of Eq. (2.1) and multiplying on the left by $\mathbf{f}'$. This shows that $\mathbf{HB}$ and $\mathbf{CB}$ commute, since $\mathbf{HBC} = \mathbf{CBH}$, but it does not mean that the eigenvalues of $\mathbf{HB}$ (i.e., ω_n) are the same as those of $\mathbf{CB}$ (i.e., λ_n) since these two operators are distinct. A similar proof was obtained by Breuer and Sirovitch (1991), but here we capitalize on the conservative properties of the dynamical system to simplify the analysis, since an explicit orthogonal relationship is available.

If the small-amplitude wave activity is reasonably conserved, then the normal modes of a linear system can be estimated from data. The quality of this estimation depends on how long the time series is relative to the timescale of the dynamical phenomenon under study. Even in the weakly nonlinear limit, this approach is still useful since the ENMs are more physically balanced than ordinary EOFs (e.g., when the covariance matrix is constructed from the geopotential). Thus, each ENM found is nearly a solution of the dynamical equation. In other words, the ENMs generated using the wave activity are dynamically balanced, whereas the physical interpretation of ordinary EOFs is difficult to find. Note that for a fixed truncation, the ENMs do not form the most efficient basis in order to explain the variance of a field $\mathbf{f}'(\mathbf{x}, t)$. The presence of $\mathbf{B}$ in the definition of the matrix $\mathbf{K}(\mathbf{x}, \mathbf{y})$ spoils this interpretation. In practice, however, the compaction efficiency of ENMs is just slightly lower than that of EOFs.

Realistic atmospheric time series are, in general, nonlinear, dissipative, and randomly forced. A way to accommodate the ENM analysis with randomness and dissipation is to add damping and random forcing to the dynamics. It is interesting to study how the principal components and the spatial part of the ENMs are modified when these are taken into account. A simple stochastic modeling of Eq. (2.1) can be obtained by adding these to the evolution equation:

$$\frac{\partial \mathbf{f}'}{\partial t} = i\mathbf{HBf}' - \gamma \mathbf{f}' + \boldsymbol{\epsilon}, \tag{2.6}$$

where $\mathbf{H}$ and $\mathbf{B}$ are Hermitian and time independent, and $\boldsymbol{\epsilon}$ and γ are uncorrelated (in time) random forcing (e.g., a Wiener process) and a Rayleigh damping coefficient, respectively. {Note that topographic forcing is not, in general, a Wiener process when the basic wind over topography is time independent, and that a special treatment is needed in order to incorporate its effects [see Eq. (2.17)]. On the other hand, a turbulent wind over a mountain ridge causes a forcing that can be considered to be a Wiener process. Note also that the forcing $\boldsymbol{\epsilon}$ can be a function of length scale.}

The normal modes $\mathbf{f}'_n$ of Eq. (2.2) are the eigenvectors of $\mathbf{HB}$ and form a complete basis. Now, expanding a solution of Eq. (2.6) in terms of the normal modes $\mathbf{f}'(\mathbf{x}, t) = \Sigma\, a_n(t)\mathbf{f}'_n(\mathbf{x})$, keeping in mind that the principal components a_n are not monochromatic any more, and projecting Eq. (2.6) on a normal mode, one gets an equation governing the principal components:

$$\frac{da_n}{dt} = (i\omega_n - \gamma)a_n + \epsilon_n, \tag{2.7}$$

where $\lambda_n \epsilon_n \equiv \int \mathbf{f}'^{\dagger}_n \mathbf{B} \boldsymbol{\epsilon}\, d\mathbf{x}$. In Fourier space, $\tilde{a}_n = (2\pi)^{-1} \int a_n e^{-i\omega t}\, dt$ and the previous equation reduce to

$$\tilde{a}_n = \frac{\tilde{\epsilon}_n}{i(\omega - \omega_n) + \gamma}. \tag{2.8}$$

The orthogonality of the principal components is recovered because

$$\begin{aligned} \int a_n a_m^*\, dt &= 2\pi \int \tilde{a}_n \tilde{a}_m^*\, d\omega \\ &= 2\pi \int \frac{\tilde{\epsilon}_n \tilde{\epsilon}_m^*}{(i\omega - i\omega_n + \gamma)(-i\omega + i\omega_m + \gamma)}\, d\omega \\ &= 0 \end{aligned} \tag{2.9}$$

when $m \neq n$. The last equality stems from the fact that the random forcing components $\tilde{\epsilon}_n$ are uncorrelated in time. It is then straightforward to show that the same eigenvalue problem as in Eq. (2.4) must be solved in order to obtain the ENMs. This means that the presence of random forcing and Rayleigh dissipation does not alter the spatial distribution of the ENMs and that the noisy part of the signal is felt only in the principal components (when the ENM method is used to analyze the output of a numerical model, the numerical artifacts will thus be seen in the principal components and not in the spatial parts). This result holds even when the random forcing is a function of length scale since the only restriction on $\boldsymbol{\epsilon}$ is that it is uncorrelated in time.

This shows that, in principle, the spatial parts of the ENM decomposition will be robust to the presence of noise. This asymmetry between time and space representation suggests that the ENM method could be a real advantage when studying noisy and dissipative dynamical systems. A straightforward time Fourier analysis is not very efficient in extracting noisy nonmonochromatic normal modes, especially when the level of dissipation and the overlapping between normal mode spectra are important. Note that a method that depends on the temporal sequence of a time series for extracting normal modes (like Fourier analysis) is subject to failure under a random reordering of the same time series. The ENM approach is unaffected by a random reordering, since Eq. (2.3) is invariant under this operation, hence showing how well the dynamics is already embedded in it.

The model equations used to construct the bilinear form of the wave activity are the unforced, conservative, primitive equations in isentropic coordinates:

$$a\cos\phi\frac{\partial u}{\partial t}+\left(\frac{1}{2}u^2+\frac{1}{2}v^2+M\right)_\lambda-a\cos\phi v\xi=0 \quad (2.10a)$$

$$a\frac{\partial v}{\partial t}+\left(\frac{1}{2}u^2+\frac{1}{2}v^2+M\right)_\phi+au\xi=0 \quad (2.10b)$$

$$a\cos\phi\frac{\partial\sigma}{\partial t}+(\sigma u)_\lambda+(\sigma v\cos\phi)_\phi=0 \quad (2.10c)$$

$$\frac{\partial M}{\partial\theta}=c_p\left(\frac{p}{p_r}\right)^\kappa \quad (2.10d)$$

$$\frac{\partial p}{\partial\theta}=-g\sigma, \quad (2.10e)$$

where σ is the isentropic density, $M=c_pT+\Phi$ the Montgomery function (T is the temperature and Φ is the geopotential), θ the potential temperature and also the vertical coordinate, a the constant radius of the earth, p_r a constant reference pressure,

$$\xi=f+\frac{v_\lambda}{a\cos\phi}-\frac{(u\cos\phi)_\phi}{a\cos\phi}$$

the vertical component of absolute isentropic vorticity, λ the longitude, and ϕ the latitude [see Andrews et al. (1987) for more details]. Subscripts in λ and ϕ denote partial derivatives with respect to these variables. We then expand the fields about a basic state $\mathbf{f}_0$, which is at least time invariant, and a solution of the primitive equations. It is then possible to find finite-amplitude wave activities that are globally conserved and of the order of the square of the perturbation fields in the small-amplitude limit (see Haynes 1988). In this diagnostic study, we will focus on the small-amplitude case for the sake of simplicity. Once linearized, it is not difficult to show that Eq. (2.10) can conserve two local wave activities that are related to symmetries of the basic state. More precisely, nonlocal wave activities can also be found even when the basic state has no space–time symmetry (T. Warn 1998, personal communication). If $\mathbf{f}_0$ is zonally symmetric, this leads to a conservation law for the pseudomomentum density J:

$$a\frac{\partial J}{\partial t}+\left[\frac{u_0J}{\cos\phi}+\frac{\sigma_0}{2}(u'^2-v'^2)+\frac{c_p\kappa}{2gp_0}\left(\frac{p_0}{p_r}\right)^\kappa p'^2\right]_\lambda$$
$$+\frac{1}{\cos\phi}(\sigma_0u'v'\cos^2\phi)_\phi+\left(-\frac{p'}{g}M'_\lambda\right)_\theta=0, \quad (2.11)$$

where $J=\sigma'u'\cos\phi-a\cos\phi\sigma_0^2(2\partial P_0/\partial\phi)^{-1}P'^2$, and $P=\xi/\sigma$ is the Ertel potential vorticity. When Eq. (2.11) is zonally averaged,

$$a\frac{\partial\bar{J}}{\partial t}+\frac{1}{\cos\phi}(\sigma_0\overline{u'v'}\cos^2\phi)_\phi+\left(-\overline{\frac{p'}{g}M'_\lambda}\right)_\theta=0, \quad (2.12)$$

and the flux is the Eliassen–Palm flux in isentropic coordinates.

The conserved local quantity that is related to the invariance of the basic state under time translation is called the pseudoenergy, and its density is A. The small-amplitude form is easily obtained from a linearization of Eq. (2.10) [see Haynes (1988) for the finite-amplitude form] and is written

$$a\cos\phi\frac{\partial A}{\partial t}+\frac{\partial F^{(\lambda)}}{\partial\lambda}+\frac{\partial}{\partial\phi}(F^{(\phi)}\cos\phi)+\frac{\partial F^{(\theta)}}{\partial\theta}=0, \quad (2.13)$$

where

$$A=\frac{\sigma_0}{2}u'^2+\frac{\sigma_0}{2}v'^2+\sigma'(u_0u'+v_0v')$$
$$+\frac{\sigma_0}{2}\frac{d\psi_0}{dP_0}P'^2+\frac{c_p\kappa}{2gp_0}\left(\frac{p_0}{p_r}\right)^\kappa p'^2 \quad (2.14a)$$

$$F^{(\lambda)}=B'_e(\sigma_0u'+\sigma'u_0)+\frac{u_0\sigma_0}{2}\frac{d\psi_0}{dP_0}P'^2 \quad (2.14b)$$

$$F^{(\phi)}=B'_e(\sigma_0v'+\sigma'v_0)+\frac{v_0\sigma_0}{2}\frac{d\psi_0}{dP_0}P'^2 \quad (2.14c)$$

$$F^{(\theta)}=-\frac{a\cos\phi}{g}M'\frac{\partial p'}{\partial t} \quad (2.14d)$$

$$B'_e=u_0u'+v_0v'+M', \quad (2.14e)$$

where B'_e is the perturbed Bernoulli function. Here ψ_0 is the preserving mass streamfunction defined by

$$u_0\sigma_0=-\frac{1}{a}\frac{\partial\psi_0}{\partial\phi} \quad (2.15a)$$

$$v_0\sigma_0\cos\phi=\frac{1}{a}\frac{\partial\psi_0}{\partial\lambda}. \quad (2.15b)$$

The given pseudoenergy is not properly conserved when the bottom boundary is not an isentrope, as it can be seen from Eq. (2.13). The contribution from the bottom boundary to the pseudoenergy should be taken into ac-

count using the conservation of potential temperature at the surface. Here, we will consider a basic flow that is zonally symmetric ($v_0 = 0$). In linear form, this gives

$$\frac{\partial \theta_s'}{\partial t} + \frac{u_{0s}}{a\cos\phi}\frac{\partial \theta_s'}{\partial \lambda} + \frac{v_s'}{a}\frac{\partial \theta_{0s}}{\partial \phi} = 0. \tag{2.16}$$

The subscript s means that the fields are evaluated at the surface. In θ coordinates, the linearization allows us to evaluate the fields at $\theta = \theta_{0s}$. After some algebra, and using the Lorenz relationship (Lorenz 1955) $p' = g\sigma_0\theta'$ at the surface, it can be shown that the globally conserved pseudoenergy density should be written

$$E = A - 2\beta\delta(\theta - \theta_{0s}), \tag{2.17}$$

when the basic flow is zonally symmetric. Here $\delta(\theta - \theta_{0s})$ is the Dirac distribution and

$$\beta = \sigma_0 u_0 u' \theta_s' + \frac{aP_0\sigma_0^2 u_0 \theta_s'^2}{2\dfrac{\partial \theta_{0s}}{\partial \phi}}.$$

The perturbed potential temperature must then be considered as a dynamic variable in the definition of the wave vector $\mathbf{f}'$.

In order to linearize the equations of a dynamical system, the choice of a basic state is crucial. Usually, when a flow is forced by topography, lee waves appear, and zonal symmetry is not observed at scales of the order of the orography. Thus, time independence of the basic state is the only symmetry that we will impose. Pseudoenergy will be used to construct the $\mathbf{K}$ matrix, and the $\mathbf{B}$ matrix is found from Eq. (2.14). The pseudoenergy density may be written

$$A = \mathbf{f}'^{\dagger}\mathbf{B}\mathbf{f}', \tag{2.18}$$

where

$$\mathbf{f}' = \begin{pmatrix} u' \\ v' \\ \sigma' \\ P' \\ p' \end{pmatrix} \tag{2.19}$$

and

$$\mathbf{B} = \begin{pmatrix} \frac{\sigma_0}{2} & 0 & \frac{u_0}{2} & 0 & 0 \\ 0 & \frac{\sigma_0}{2} & \frac{v_0}{2} & 0 & 0 \\ \frac{u_0}{2} & \frac{v_0}{2} & 0 & 0 & 0 \\ 0 & 0 & 0 & \frac{\sigma_0}{2}\frac{d\psi_0}{dP_0} & 0 \\ 0 & 0 & 0 & 0 & \frac{\kappa c_p}{2gp_0}\left(\frac{p_0}{p_r}\right)^{\kappa} \end{pmatrix}. \tag{2.20}$$

This system is overspecified since we should need only three independent components in the definition of $\mathbf{f}'$ due to the fact that the primitive equations in hydrostatic form comprise three prognostic equations and two diagnostic equations. This overspecification does not cause any problem if consistency among variables is verified. Furthermore, it allows the matrix $\mathbf{B}$ to be written in a very simple form without any differential or integral operators. Note that $\mathbf{B}$ is singular when $d\psi_0/dP_0$ changes sign within the domain, hence the possibility of having modal instability as expected from linear theory.

In practice, data are usually not available on isentropic levels but rather in pressure coordinates. Modifications described in Andrews (1987) for the expression of the wave activity must then be employed. The transformations are given in the appendix.

3. The dataset

The output of the troposphere–stratosphere–mesosphere GFDL SKYHI general circulation model (Fels et al. 1980; Mahlman and Umscheid 1984; Miyahara et al. 1986; Hayashi et al. 1989; Hamilton 1995; Hamilton et al. 1995) was analyzed using the present method. At a horizontal resolution of 1° of latitude by 1.2° of longitude, with 40 vertical levels (from the surface up to about 80 km), and an explicit leapfrog time differencing with time steps of 60 s, five days of data sampled hourly were diagnosed for the virtual period 25 December 1983 to 29 December 1983, inclusively (model calendar). Given this grid resolution, one must be aware that for characteristic wind speeds of the order of 10 m s^{-1}, wave motions with timescales less than $\sim 10^4$ s cannot be resolved. Thus, inertia–gravity waves occur at the fast limit of the temporal resolution of the model.

We have limited our analysis to three windows: one located over the Rocky Mountains in the western part of North America with area of 4800 km × 2400 km (the center of the grid is at 46.4°N and 114.6°W), another over the Pacific Ocean at midlatitudes, also with area of 4800 km × 2400 km (and the center of the grid at 46.4°N and 174.6°W), and a third one in a tropical region over Central America with area of 6900 km × 3450 km (center of the grid at 20.0°N and 90.0°W). This was done in order to contrast mountainous, nonmountainous, and tropical locations. The analyses were performed in two parts: a first analysis between 618 and 3.9 hPa dealing with the troposphere up to the midstratosphere, and a second analysis between 62 and 0.03 hPa dealing with the upper part of the middle atmosphere (stratosphere and mesosphere). Typical profiles of the time mean of the squared buoyancy frequency and zonal velocity for the three analyzed regions are shown in Fig. 1.

The fact that we restrict the analyses to limited domains may violate wave-activity conservation laws even

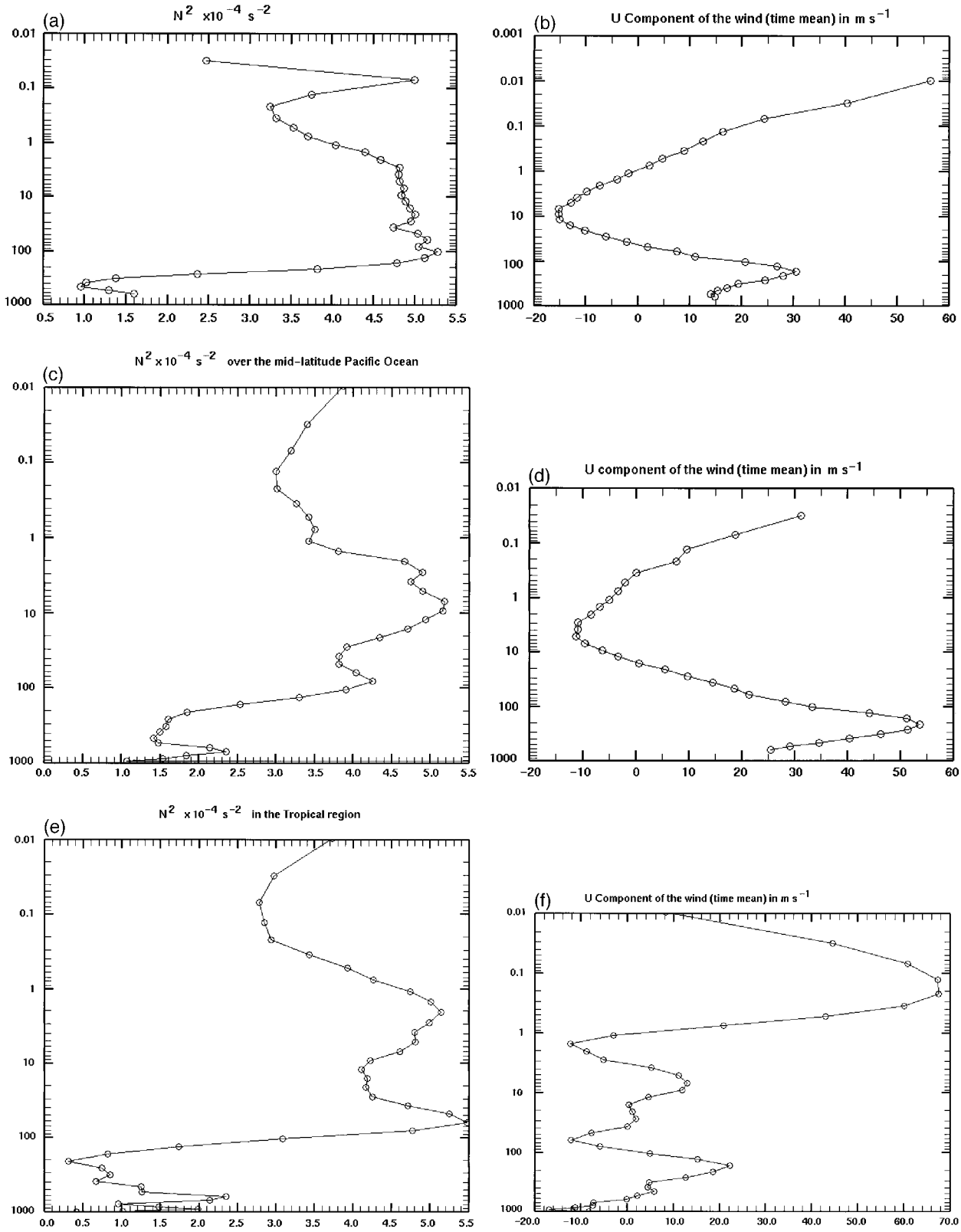

FIG. 1. (a) Time mean (over five days) of the square of the buoyancy frequency calculated at 43°N and 100°W over North America. (b) The same as in (a) except that the mean zonal wind is shown. (c) Time mean (over five days) of the square of the buoyancy frequency calculated at 43°N and 168°E over the Pacific Ocean. (d) The same as in (c) except that the mean zonal wind is shown. (e) Time mean (over five days) of the square of the buoyancy frequency calculated at 10°N and 90°W over Central America. (f) The same as in (e) except that the mean zonal wind is shown.

when dissipation and forcing are absent. This is due to nonvanishing Eliassen–Palm (or more generally wave activity) fluxes across the boundary. In practice, however, this does not seem to cause serious problems since a wave with a sufficient number of oscillations inside the domain will contribute significantly to the statistics and its modal structure will be represented quite well even though a related nonvanishing wave-activity flux may exist across the boundary.

4. Results

In the present study, the basic state is taken to be the time mean of the time series. This means that waves with period greater than 5 days (including zero phase speed waves) will contribute to define the basic state. In order to assess the relative importance of stationary gravity waves (mainly excited by orography and not described by the present ENM analysis) versus transient waves, the standard deviation of the horizontal divergence of the velocity field is calculated over the Rockies. The horizontal divergence is utilized in order to filter out rotational modes. We will then proceed to the ENM analysis.

Note that by taking the basic state to be a time average, it is not necessarily a solution of the nonlinear evolution equation. However, this time average is found in the present work to be fairly zonally symmetric, and hence the unbalanced terms of the basic state can be considered negligible.

a. The horizontal divergence field over the Rockies

At midlatitudes, the horizontal divergence of the velocity field can reveal dominating inertia–gravity modes. It appears that these are most easily seen using this field since rotational modes are then filtered out. Figures 2a and 2b show the time average of $\nabla_H \cdot \mathbf{v}$, and Fig. 2c shows a vertical profile of its standard deviation at a point over the Canadian Rockies at 50°N and 120°W (this location is representative of the gravity wave dynamics over the Rockies, and Fig. 2c is generic). This indicates that the transient component of the gravity wave signal is dominant in the upper stratosphere and in the mesosphere, and that the stationary component is more important in the troposphere. In the lower stratosphere (from 200 to 10 hPa), the transient and stationary components are more or less of the same magnitude. Here, the relative magnitude of the stationary and transient components of the gravity wave signal is measured by the ratio of the time mean with the standard deviation at 50°N and 120°W. Part of the stationary wave packet energy is found to be absorbed in the vicinity of the lowest critical level $ku_0 = f$ (the so-called Jones' critical level; Jones 1967; Grimshaw 1975; Wurtele et al. 1996) near 20 hPa, where f is the Coriolis parameter, k is the dominant horizontal wavenumber ($\sim 2\pi/600$ km, or $\sim 6\Delta x$) measured directly from the divergence field, and u_0 is the background wind at 20 hPa (~ 10 m s^{-1} at 50°N and 120°W, not shown). Interestingly, the vast majority of gravity wave absorption events observed in this study occur near Jones' critical levels (recall that these are not located where the wave phase speed matches the background wind, but rather where the absolute value of the inertia–gravity wave intrinsic fre-

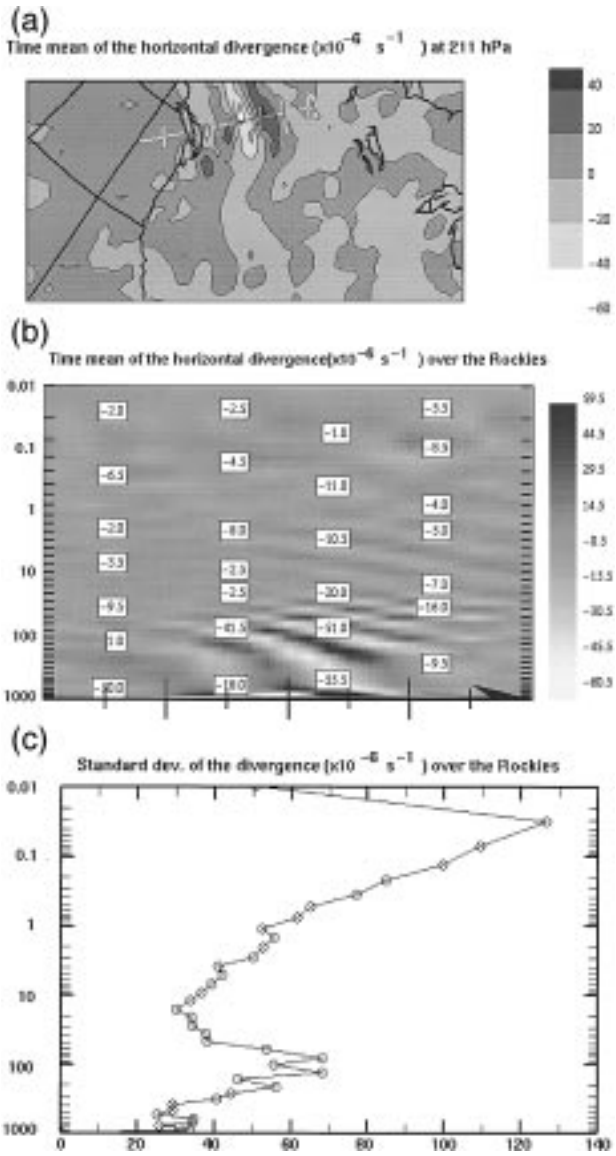

FIG. 2. (a) Time mean of the horizontal divergence of the velocity field obtained from the GFDL SKYHI model for the virtual time 0000 MT (model time) 25 December 1983 to 2300 MT 29 December 1983 at 211 hPa. The arrow indicates the line where a vertical cut has been taken (see Fig. 2b). The center of the depicted region is at 46.4°N and 114.6°W. (b) Vertical cut of the wave shown in Fig. 2a taken from 45°N and 130°W to 55°N and 110°W. (c) Vertical profile of the standard deviation of the velocity horizontal divergence at 50°N and 120°W.

quency matches the absolute value of the Coriolis frequency). Figure 2c also indicates that part of the transient component is absorbed near 20 hPa at 50°N and 120°W. This can be caused by the absorption of propagating mountain waves generated by the temporal fluctuations of the large-scale flow [see section 4b(2)i]. In order to verify if these waves are real phenomena and not artifacts of the model, an analysis using hodographs has been performed on the propagating part of the signal and it showed that the dispersion relation for inertia–gravity waves is obeyed within 12% (Charron 1998).

From the point of view of wave–mean flow interactions, a Jones' critical level acts on a monochromatic inertia–gravity wave somewhat similarly as an ordinary critical level ($c = u_0$) acts on a monochromatic pure gravity wave (neglecting rotation). In the case of a continuous spectrum, Wurtele et al. (1996) state that wave absorption and nonlinear effects do not occur in the presence of multiple Jones' critical levels, even though vertical propagation is inhibited. In the absence of dissipation, this seems counterintuitive since weak nonlinearities are expected (in the form of energy exchange between the waves and the mean flow) in order to avoid energy accumulation under the zero background wind level. This should be addressed specifically but is beyond the scope of the present work.

It is interesting to understand what are the sources of the propagating gravity wave signal (the gravity waves that are not stationary mountain waves). The time dependence of the surface wind blowing across the mountain range can explain part of the gravity wave spectrum, but as it will be seen later, the jet stream is also thought to be a source of inertia–gravity waves (IGWs). It was not possible to identify IGWs emerging from the jet stream using the horizontal divergence of the velocity field, even though the empirical normal mode analysis revealed that gravity wave activity was initiated at the jet stream level (see sections 4b,c). The signature of IGWs generated by the jet stream, when using $\nabla_H \cdot \mathbf{v}$, could be undetectable because those waves are very weak compared with the orographic gravity waves near the tropopause.

b. The ENM analysis

As a first attempt to extract inertia–gravity modes from the simulated dynamical system, we used a simplified version of the ENM theory described above: the basic wind in the matrix $\mathbf{B}_{(p)}$ (see the appendix) has been put to zero, which reduces the pseudoenergy to the wave energy. This simplification is based on the previous analysis of Brunet and Vautard (1996), showing that for large wavenumbers ($s > 4$, where s is the zonal wavenumber), the empirical modes obtained from the full ENM analysis are very similar to those obtained by defining the basic wind to be a solid-body rotation. In this study, we will then neglect shear processes in the matrix $\mathbf{B}_{(p)}$ when establishing the dynamical basis. Despite this simplification, we expect that this approximation is quite reasonable for the high-wavenumber structures obtained in this work. It is important to understand that neglecting spatial variations of the basic flow in the matrix $\mathbf{B}_{(p)}$ does not mean that the empirical modes will not ''feel'' the presence of the actual background flow (e.g., the impact of critical levels); it simply means that the method may not be as accurate in isolating or separating normal modes when their length scales are of the same order as the length scale of the background spatial variation. Also, if critical levels only influence wave propagation at their vicinity (and not all over the analyzed domain), it is expected that wave energy (instead of pseudoenergy) could be used in order to define the modes orthogonal relationship since the ''volume'' of the critical layers can be considered small as compared to the entire volume of the analyzed domain. We will examine in a subsequent study the impact of this simplification on the diagnostic results.

1) THE PRINCIPAL COMPONENTS

In the present analysis, the bandwidth of the PCs is narrow, as can be seen in Fig. 3, and one would be tempted to conclude that the linear nature of the dynamics is important. However, amplitude modulation is still present in many of the PCs.

Figure 4 shows the distribution of absolute wave periods weighted by the relative norm

$$N_n = \frac{\int d\mathbf{x}\mathbf{f}_n'^{\dagger}\mathbf{f}_n'}{\sum_m \int d\mathbf{x}\mathbf{f}_m'^{\dagger}\mathbf{f}_m'}$$

for all the modes. From now on, and for the rest of the text, this norm will be called the ''variance.'' Note that under this norm the ENMs are not orthogonal. Here, the period of a mode is taken to be the period at which the spectrum of its associated PC is maximum. It is seen that the high-frequency wave spectrum (periods lower than 12 h) dominates the low-frequency wave spectrum (periods greater than 12 h) in the mesosphere of the tropical region, and that the portion of the signal explained by high-frequency waves is similar for oceanic and mountainous regions at midlatitudes. The Tropics is the only analyzed region where a dominance of high-frequency waves over low-frequency waves is observed. Note that the peaks with period greater than about 20 h could not be representative of the exact period of their associated modes since the time series is only 120 h long.

2) THE THREE-DIMENSIONAL WAVE STRUCTURES

(i) Mountainous region

Over the Rockies in the troposphere, the modes explaining the most variance are evidently those asso-

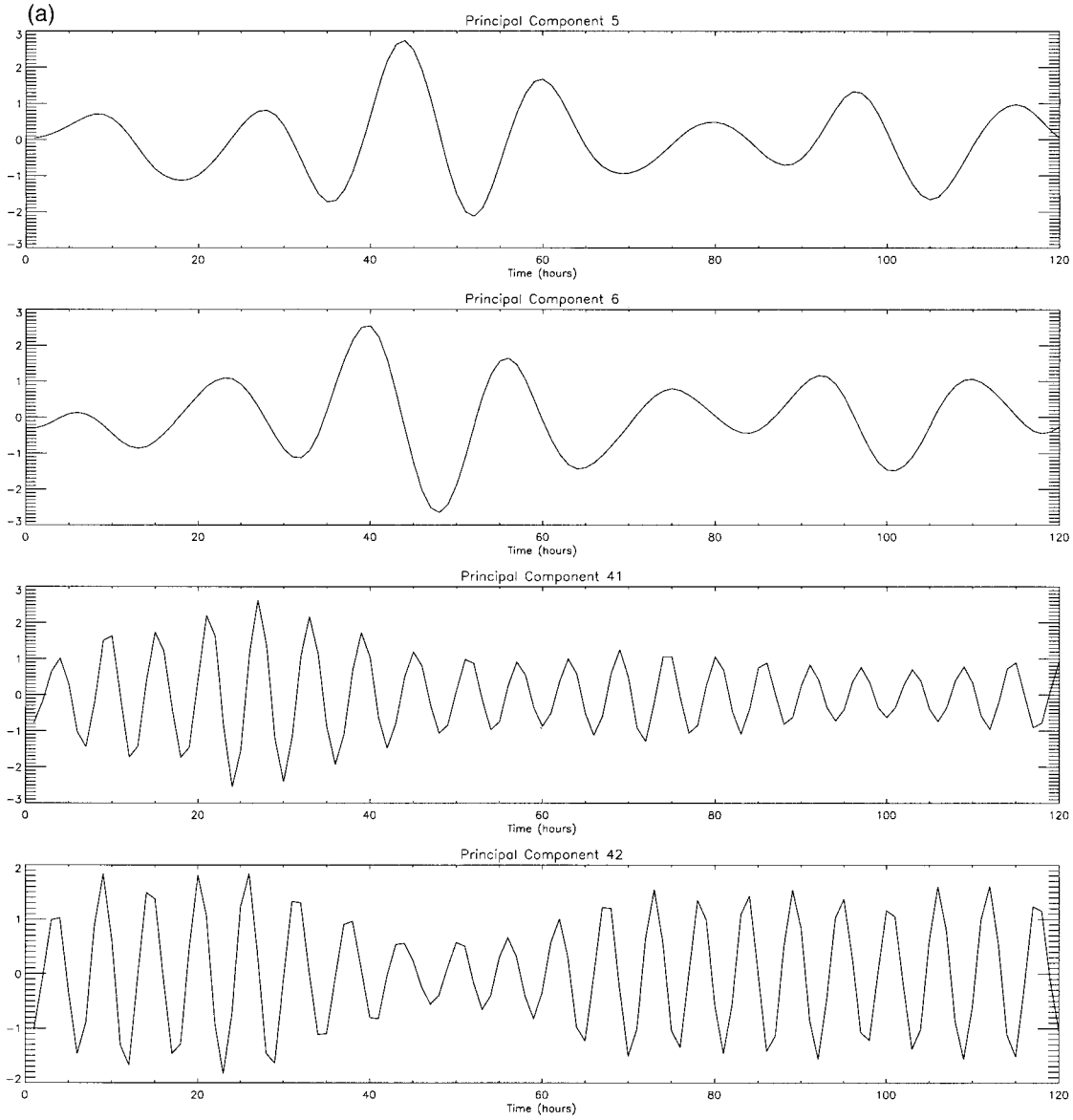

FIG. 3. (a) Time series of some selected principal components of the GFDL SKYHI model for the analysis made over the Rockies from 618 to 3.9 hPa. Modes 5 and 6 are associated with Rossby wave propagation (they are in quadrature), and modes 41 and 42 describe inertia–gravity modes. Mode numbers refer to their importance in explaining the variance of the signal.

ciated with Rossby waves. Figures 5a,b show the horizontal and vertical structure of the second mode in importance out of 120. It represents a vertically evanescent Rossby wave with zonal wavenumber of about 7. In our stratosphere and mesosphere analysis, Rossby waves of zonal wavenumber equal to or greater than 4 are almost absent due to their absorption in the lower stratosphere (Charney and Drazin 1961). The first modes that we have observed in the middle atmosphere have large-scale structures that show no evidence of coherence and propagation. This is certainly due to the fact that the window size is too small to resolve stratospheric planetary Rossby waves. However, in the stratosphere, localized structures with a much finer scale can be observed in the leading empirical normal modes. These structures seem to be associated with westward-propagating gravity waves relative to the mean flow (see Fig. 6 for an example) with relatively high vertical wavenumbers. These wavy structures could be related to a slow temporal modulation of the quasi-stationary mountain waves described earlier and depicted in Figs. 2a and 2b.

A time-dependent incident wind on a mountain ridge can generate propagating gravity waves (Lott and Tei-

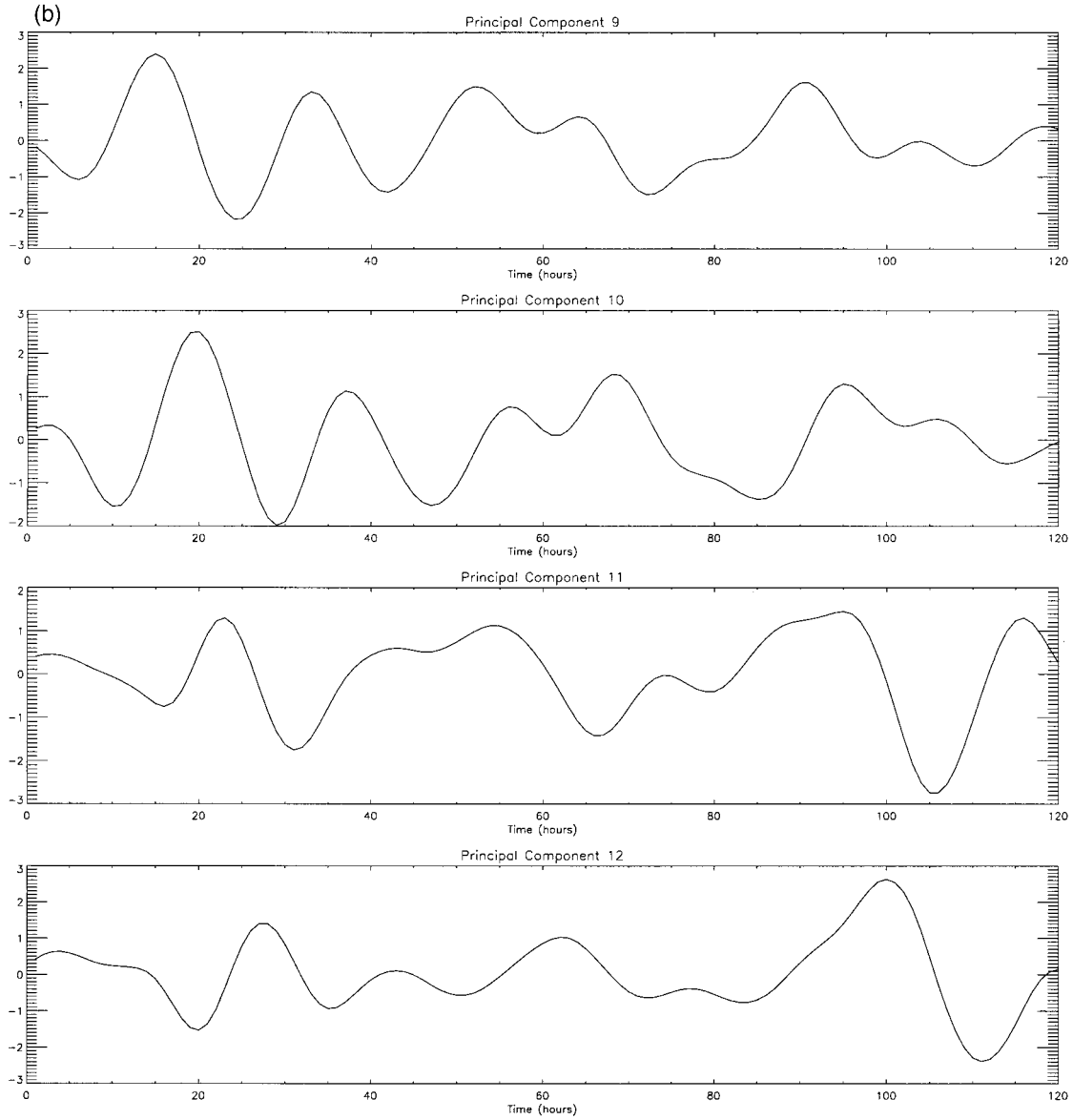

FIG. 3. (*Continued*) The total number of modes is 120. (b) Time series of some selected principal components of the GFDL SKYHI model for the analysis made over the Tropics from 62 to 0.03 hPa. Note that the PC spectra are less narrow than in Fig. 3a.

telbaum 1993). In the present case, even if the basic wind used in the diagnosis analysis is taken to be time independent, the large-scale flow (e.g., long Rossby waves) is still time dependent and can excite phase-propagating inertia–gravity waves. Figure 7 shows the time evolution of the wind just west of the Rockies (at 45°N) near the surface. Propagating mountain waves could possibly be produced in the present simulation. Figure 8 shows a propagating mode that is going eastward (this mode has been obtained by doing a separate analysis ranging from 973 to 81 hPa). It is absorbed in the upper troposphere where it encounters its lowest Jones' critical level. Actually, most of the propagating mountain waves diagnosed are absorbed in the upper troposphere and do not propagate into the middle atmosphere. It was observed in this analysis that most of the westward- (eastward-) propagating tropospheric inertia–gravity waves were located on the west (east) side of the Rockies.

An interesting feature of the 3D modes is that the origin of the propagating waves can sometimes be traced back and thus can give useful information about moving gravity wave sources (these sources are needed in a realistic parameterization of gravity wave drag), if the

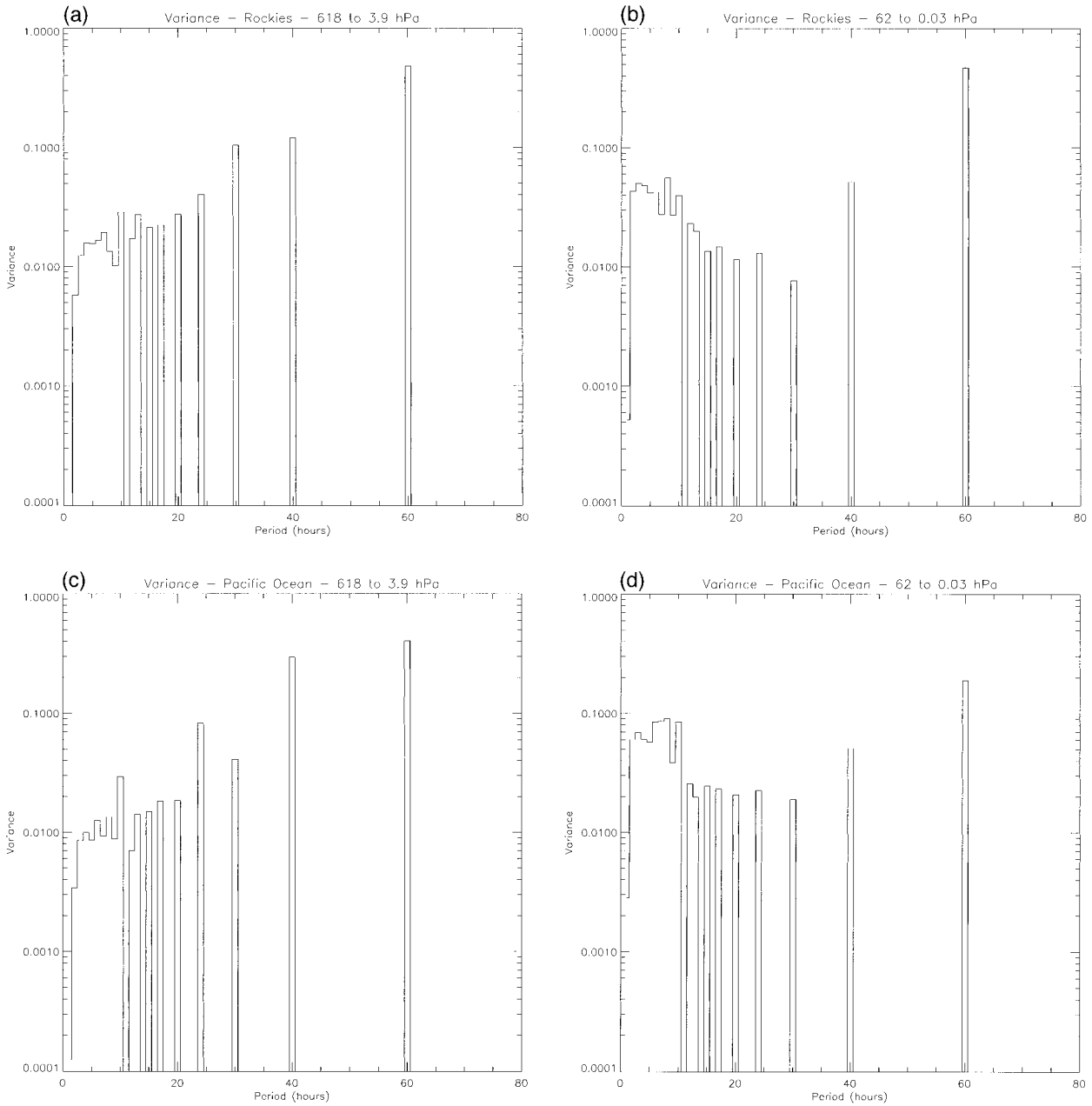

FIG. 4. (a) Distribution of absolute wave periods weighted by the variance explained by each mode (from 618 hPa to 3.9 hPa) over the Rockies. (b) The same as (a) but from 62 to 0.03 hPa. (c) The same as (a) but over the Pacific Ocean. (d) The same as (c) but from 62 to 0.03 hPa. (e) The same as (a) but over the Tropics. (f) The same as (e) but from 62 to 0.03 hPa.

length of the analyzed time series is of the same order as the mechanism producing the waves. Figure 9 shows inertia–gravity wave generation with horizontal wavelength of about 600 km and absolute period of about 3.5 h near the jet stream. This mode is the 70th out of 120. The necessary condition for instability is met near the jet (i.e., $d\psi_0/dP_0$ changes sign in the jet core). Vertical profiles of the time mean buoyancy frequency and zonal wind are shown in Figs. 1a and 1b, respectively. Sutherland et al. (1994) and Sutherland and Peltier (1995) studied gravity wave emission caused by hydrodynamic instability with similar profiles. Their analyses based on two-dimensional models show that linear processes can lead to spontaneous gravity wave generation under certain conditions. Other nonlinear mechanisms are thought to emit gravity waves (Davis and Peltier 1979; Fritts 1982, 1984), and determining a single instability mechanism responsible for the emission of the

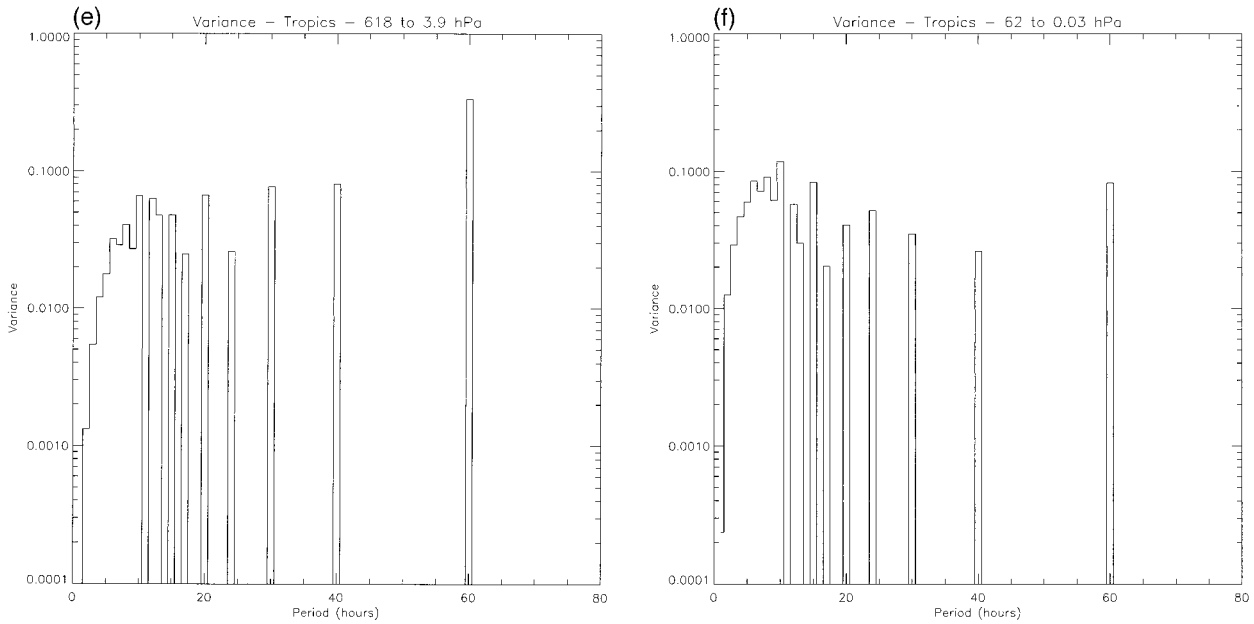

FIG. 4. (*Continued*)

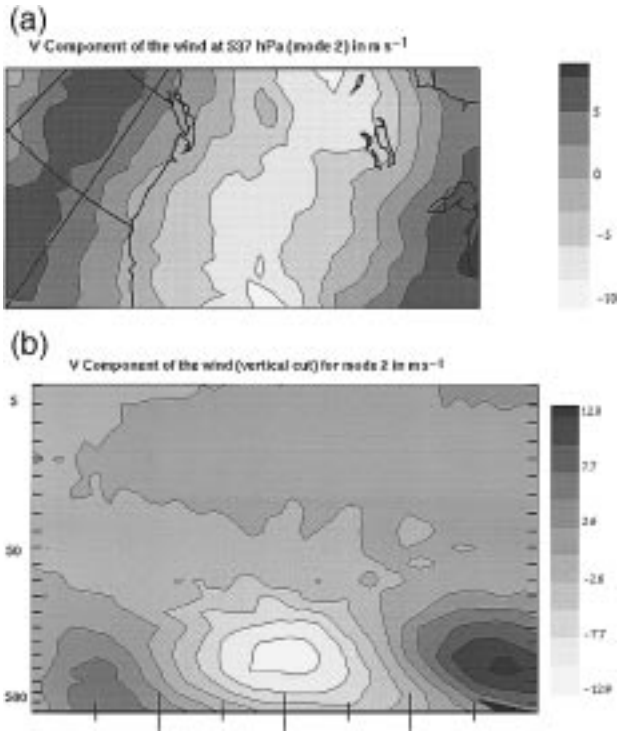

FIG. 5. (a) Horizontal cut at 537 hPa of the *V* component of the wind (on a polar stereographic grid) for the second mode in importance (out of 120) explaining 22% of the variance for the analysis of the GFDL SKYHI model. The wavelength is about 4000 km and the absolute period is around 60 h. (b) The same as in (a) except that a vertical cut of the mode is shown. This wave corresponds to a zonal wavenumber of about 7, and does not propagate into the stratosphere. The cut is taken from 42°N and 160°W to 42°N and 90°W.

mode described in Fig. 9 is not straightforward. The minimum Richardson number of the basic flow calculated in a column where inertia–gravity waves are generated is of the order of 8 (see Fig. 10a). Gravity wave generation by Richardson instabilities is thus unlikely given the present model vertical resolution. Fritts and Luo (1992) and Luo and Fritts (1993) investigated inertia–gravity wave emission by geostrophic adjustment of an idealized jet stream and studied, using linearized equations, the spontaneous radiation of inertia–gravity waves for an unbalanced initial state. O'Sullivan and Dunkerton (1995) examined the possibility of inertia–gravity wave emission near the jet stream due to an unstable baroclinic development causing geostrophic adjustment at the jet stream level. In our case, inertia–gravity wave emission near the jet stream occurs

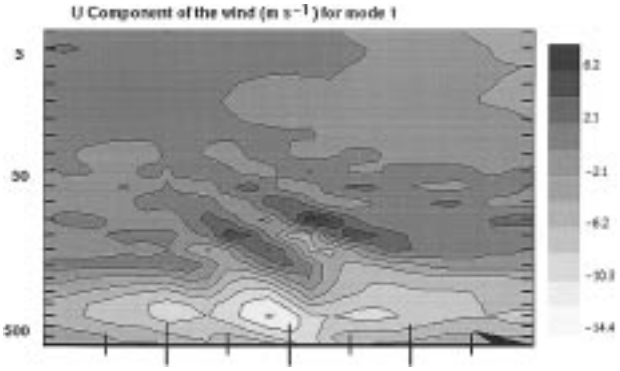

FIG. 6. Vertical cut of an inertia–gravity wave moving westward relative to the mean flow and observed in the leading empirical normal modes. The level of absorption corresponds to a critical level $\hat{\omega} = f$. The cut is taken from 45°N and 130°W to 55°N and 110°W.

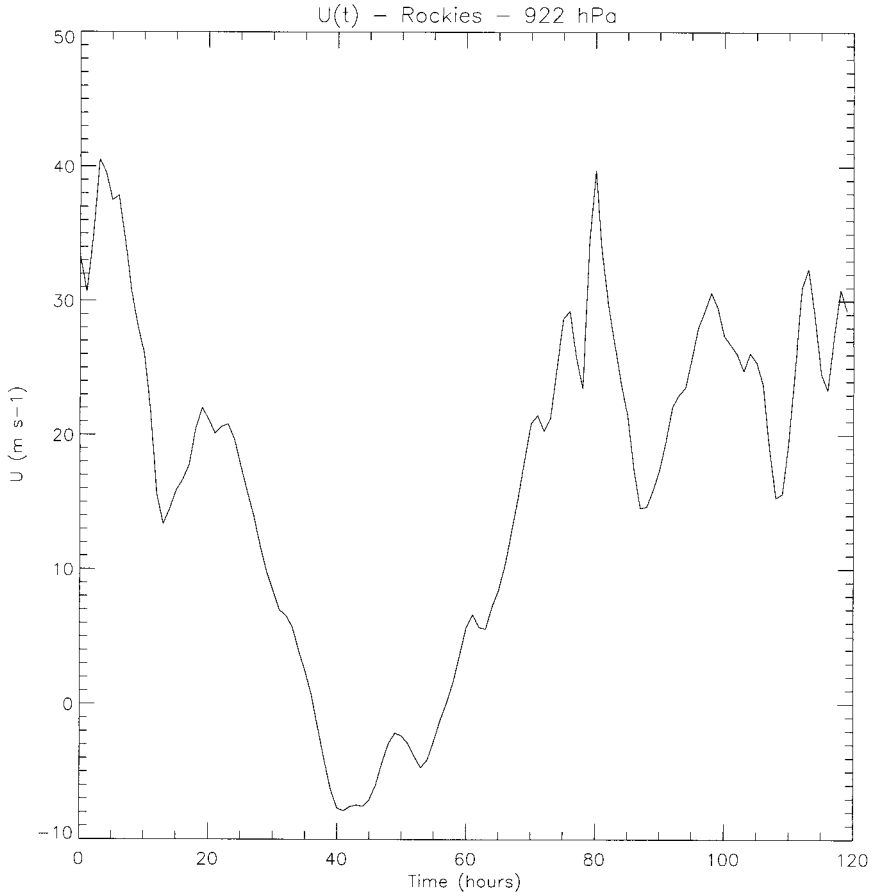

FIG. 7. The zonal wind at 922 hPa just west of the Rockies. This shows that propagating mountain waves are expected. The profile is taken at 45°N and 127°W.

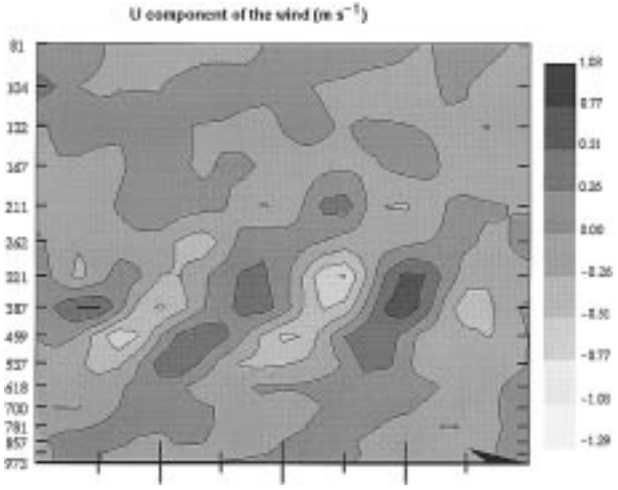

FIG. 8. Vertical cut of an eastward-propagating inertia–gravity wave in the troposphere with wavelength of 620 km and absolute period of 7.2 h and absorbed near the tropopause. This mode has been obtained by performing a separate analysis ranging from 973 to 81 hPa, and it represents 0.3% of the total variance. The cut is taken from 52.5°N and 114°W to 46°N and 88°W.

throughout the five days of analysis. Figure 10b shows a vertical cut of the time mean Rossby number Ro ($\equiv|\mathbf{v}\cdot\nabla\mathbf{v}|/|f\mathbf{v}|$) just east of the Rockies near 43°N. Peaks of Ro ~0.8 to 1.2 are frequently observed on the upper and lower flanks of the SKYHI jet stream and geo-

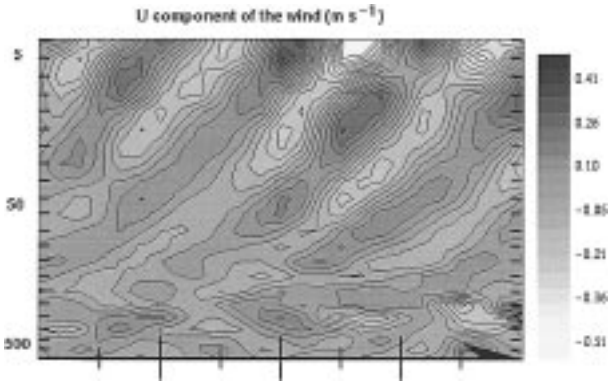

FIG. 9. Inertia–gravity wave excitation, with wavelength of 600 km and absolute period of 3.5 h, at the jet stream level. This mode is the 70th in importance out of 120. The cut is taken from 42°N and 114°W to 44°N and 90°W.

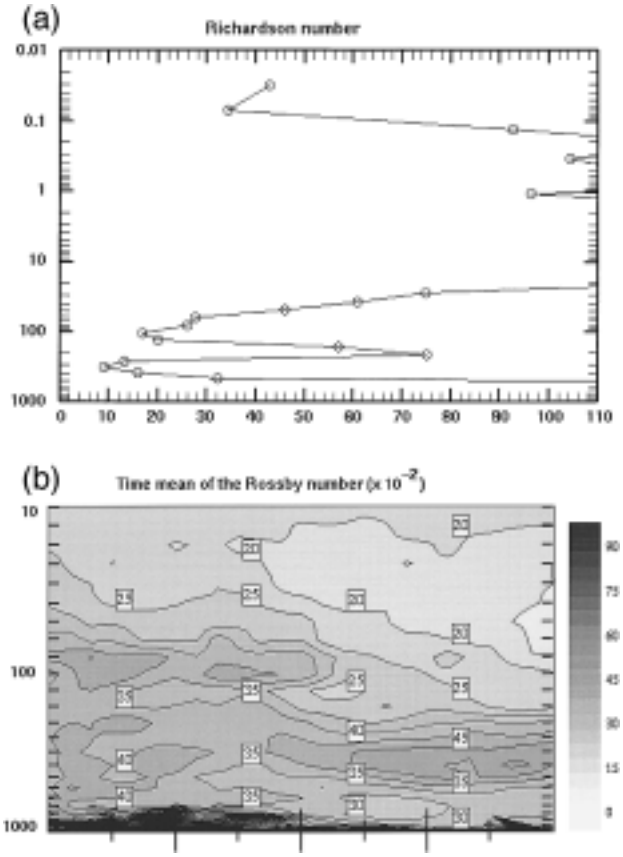

FIG. 10. (a) The Richardson number for profiles shown in Figs. 1a and 1b. (b) Vertical cut of the time mean Rossby number taken from 42°N and 114°W to 44°N and 90°W.

strophic adjustment could be expected if balanced ageostrophic motion is not prevailing. Another possibility could be that these waves are generated by a sustained nonlinear and ageostrophic jet stream flow through triad interactions. Bartello (1995) showed, using analytic arguments and numerical results, that at Rossby numbers of order 1, slow modes can interact to generate a fast mode and that geostrophic adjustment may not take place. In order to establish whether geostrophic adjustment or a sustained nonlinear and ageostrophic flow is responsible for this wave emission, a correlation between the Rossby number and the time-evolving wave energy of the modes describing waves emerging from the jet stream has been calculated. It turns out that near the jet stream, there is no clear correlation between the Rossby number and the inertia–gravity wave energy. This is an indication that geostrophic adjustment may not be responsible for the presence of these inertia–gravity waves over the jet. Since the Rossby number is relatively large throughout the five days, nonlinear downscale energy transfer as a gravity wave source cannot be excluded. In fact, a longer time series with a succession of linear and nonlinear

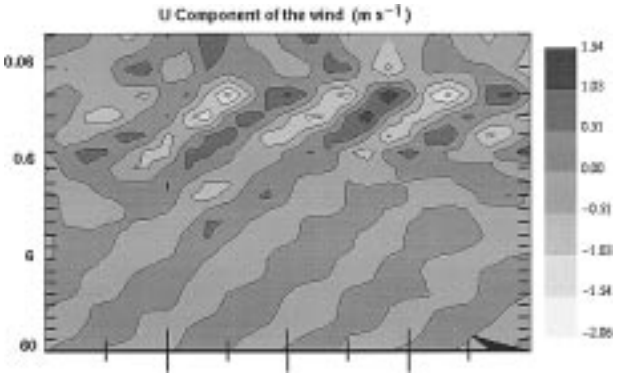

FIG. 11. Wave absorption in the mesosphere of a mode with the same characteristics as the one shown in Fig. 9 and at the same horizontal location.

regimes would be needed in order to resolve this issue. Note that other waves associated with this jet instability were observed in the middle atmospheric window and showed in some cases well-defined wave propagation and absorption at higher levels in the mesosphere. Figure 11 shows such a wave absorption near the top of the model probably caused by the lowest Jones' critical level encountered by the wave.

(ii) Oceanic region

Over the Pacific Ocean, inertia–gravity waves generated near the surface can be observed (see Fig. 12 for an example). The background flow and the wave characteristics are such that part of the wave packet reaches a Jones' critical level near 700 hPa and is absorbed there. The dynamical source of these waves could be attributed to the boundary layer instability since Richardson numbers less that ¼ (and negative) are frequently measured in the model boundary layer over the ocean.

The jet stream over the Pacific has a mean velocity

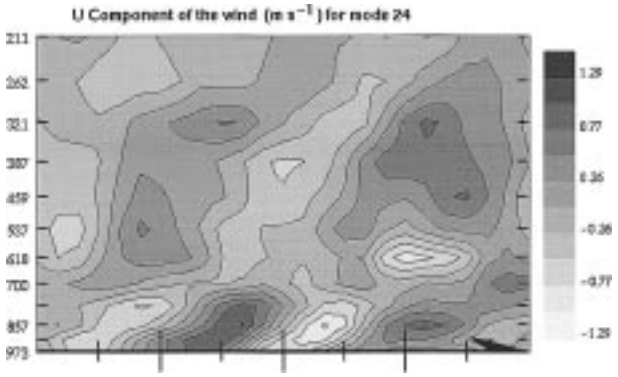

FIG. 12. Wave absorption by a Jones' critical level in the lower troposphere near 700 hPa. The horizontal wavelength is ~550 km and the absolute period is ~6 h. The vertical cut is taken from 43°N and 160°E to 43°N and 175°E. This mode was obtained from an analysis ranging from 973 to 81 hPa.

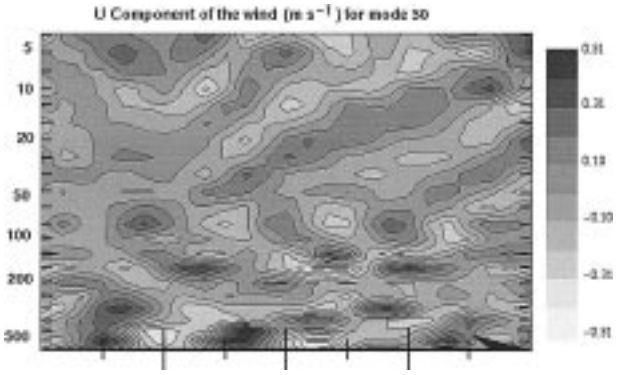

FIG. 13. Vertical cut along a latitude band of the zonal component of the wind for mode 50 showing the effect of critical levels just above the jet stream on a gravity wave with absolute period of 5 h and horizontal wavelength of 520 km. The vertical cut is taken from 40°N and 175°E to 40°N and 170°W.

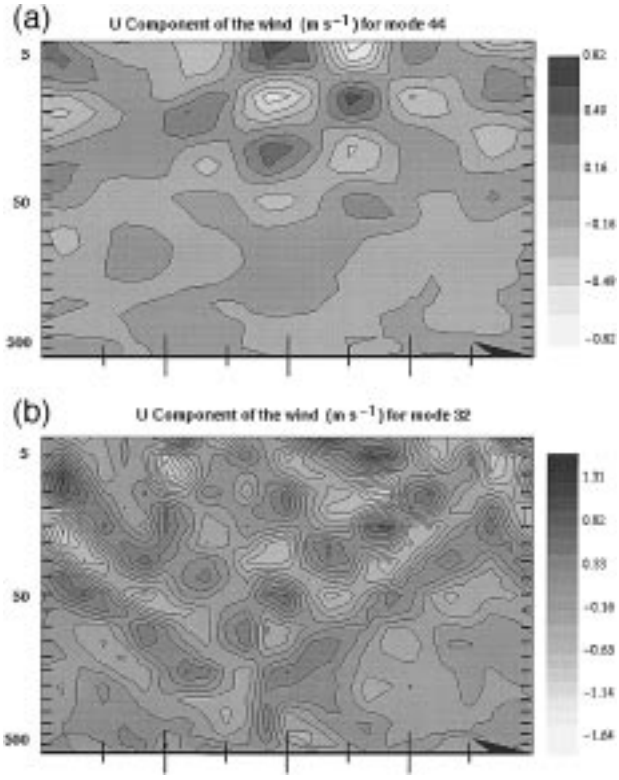

FIG. 14. (a) Standing pattern with a period of 5.5 h and horizontal wavelength of 820 km. The vertical cut is taken from 10°N and 100°W to 10°N and 80°W. (b) Symmetric pattern with a period of 7.5 h and a horizontal wavelength of 550 km. The vertical cut is taken from 10°N and 120°W to 10°N and 90°W.

that reaches a maximum value of the order of 55 m s^{-1} (see Fig. 1d) and a lot of wave absorption due to singular levels ($\hat{\omega} = \pm f$ and 0) was observed just above. This jet strength is to be compared to the ~30 m s^{-1} over the Rockies. For an inertia–gravity wave described by an absolute period of 5 h and a horizontal wavelength of 520 km, the three singular levels are approximately located between 100 and 60 hPa above the jet stream (Fig. 13). Note that a wavy pattern is located above the critical levels and amplifies with height due to non-Boussinesq effects. In this case, the critical levels in the lower stratosphere and in the troposphere make it difficult to verify if the jet stream is the source of these IGWs.

Modes 7 and 8 of the stratospheric and mesospheric analysis were observed to oscillate at the semidiurnal frequency. Their horizontal structure is too large to be fully described by the empirical modes obtained from this limited area analysis. Their vertical wavelength is about 20 km, and the amplitude of the potential temperature and wind velocity at 0.1 hPa associated with these modes are 10 K and 4 m s^{-1}, respectively. These modes describe probably thermal tides. A clear monochromatic diurnal signal was not observed in our analysis.

(iii) Tropical region

Over Central America, inertia–gravity wave activity was high during the five days of analysis. Empirical modes with IGW characteristics were found to explain at least 30% of the signal in the upper troposphere and lower stratosphere. Much of the IGWs were generated in the upper troposphere (the Richardson number was lower than 0.25 around 200 hPa on many occasions during the five days of analysis), and a significant portion of the eastward-propagating inertia–gravity waves at 10°N was found to be absorbed near the tropopause due to the presence of persistent westerlies around 200 hPa. One striking feature of the analysis made below 3.9 hPa is the monochromaticity of the modes. The first 40 modes (out of 120), when they are ordered according to their variance, are sinuslike, indicating an almost pure oscillatory regime. The most important IGW modes with wavelength greater than 1000 km were propagating westward relative to the time mean flow. Eastward-propagating IGW modes were not predominant and were not found before mode 26, but the eastward IGWs with phase speed greater than about 30 m s^{-1} were able to reach the stratosphere. Also, it was often observed that for high-frequency ENMs, the structures consisted of the superposition of a pattern tilting eastward and another tilting westward. In Fig. 14a we see such a pattern composed of two waves with opposite vertical wavenumber, but with approximately the same amplitude. Figure 14b is another example of such superposition, which could be the result of wave reflection from a height near 1 hPa, or could indicate that waves with westward and eastward tilt are generated [this last hypothesis is consistent with the basic wind showed in Fig. 1f if the ''obstacle effect'' (Clark et al. 1986) is responsible for the emission of these waves, since pos-

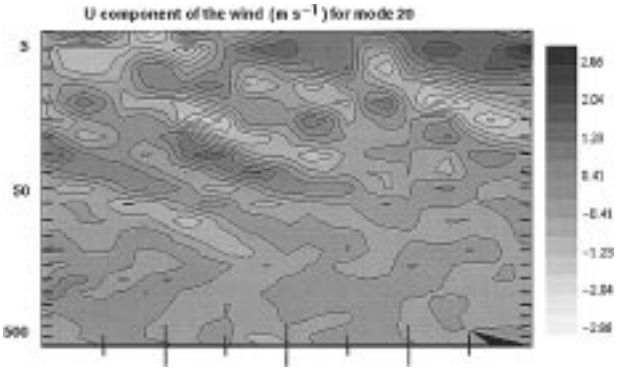

FIG. 15. Westward-propagating inertia–gravity wave with an absolute period of 12 h and a horizontal wavelength of 750 km. The vertical cut is taken from 10°N and 110°W to 10°N and 80°W.

itive and negative vertical shear are present in the time mean wind below 50 hPa]. The total momentum transported upward by the modes shown in Figs. 14a,b is almost zero since the contribution of the component with westward tilt (transporting momentum downward) is almost exactly balanced by the component with eastward tilt (transporting momentum upward). Since symmetric patterns are observed mainly in relatively high-frequency modes (with relatively low variance), the impact on the mean flow by breaking IGWs will come from relatively low-frequency IGWs, such as the one depicted in Fig. 15 that tilts westward, has a period of 12 h and a wavelength of 750 km, and is the 20th in importance out of 120.

In the tropical upper stratosphere and mesosphere, a broadening of the principal component spectra is observed for the first 20 modes (see Fig. 3b for some examples). This could indicate that shear processes may be of primary importance in the propagation of these waves, or that nonlinearities are strong, since we expect in this wave energy analysis these factors to widen the overall PC spectra. The broadening of the first 20 PC spectra could also be explained by the rather small domain size compared with Kelvin wave horizontal scales, so that nonvanishing wave-activity fluxes across the boundaries may not be negligeable. Modes 5 to 10 (not shown) represent somewhat disturbed patterns with mixed eastward and westward tilt, and a horizontal and vertical wavelength of about 2000–3000 km and ~15 km, respectively. The origin of the waves represented by these patterns is certainly located outside the analyzed window. The subsequent modes (number 20 and higher) with horizontal wavelength ranging from 600 to 1000 km have a narrow bandwidth (in their time series) and an almost pure oscillatory regime is observed. As can be seen in Figs. 4e,f, the high-frequency component of the flow is relatively more important in the upper region of the middle atmosphere.

The wave characteristics discussed in this section are summarized in Table 1.

TABLE 1. A summary of the empirical mode characteristics described in the text.

Region	Mode number	Period (h)	Wavelength (km)	Phase speed (m s^{-1})	Absorption level (hPa)
Rockies	2	60	4000	18.5	100
Rockies	1	60	600	−6.9	20
Rockies	70	3.5	600	47.6	0.1
Rockies	34	7.2	620	23.9	262
Pacific	41	6.0	550	25.5	700
Pacific	50	5.0	520	28.9	—
Tropics	44	5.5	820	±41.4	—
Tropics	32	7.5	550	±20.4	—
Tropics	20	12.0	750	−17.4	—

c. Eliassen–Palm flux divergence

The impact of individual modes on the zonal mean zonal flow and on the residual circulation can be estimated by evaluating the divergence of the Eliassen–Palm flux. In log pressure coordinates [$z \equiv -H \ln(p/p_r)$], the zonally averaged zonal momentum equation can be written using transformed Eulerian mean (TEM) variables (see Andrews et al. 1987):

$$\overline{u}_t + \overline{v}^*[(a\cos\phi)^{-1}(\overline{u}\cos\phi)_\phi - f] + \overline{w}^*\overline{u}_z - \overline{X} = (\rho_0 a\cos\phi)^{-1}\nabla\cdot\mathbf{F}, \tag{4.1}$$

where $\overline{v}^* \equiv \overline{v} - \rho_0^{-1}(\rho_0\overline{v'\theta'}/\overline{\theta}_z)_z$ and $\overline{w}^* \equiv \overline{w} + (a\cos\phi)^{-1}(\cos\phi\,\overline{v'\theta'}/\overline{\theta}_z)_\phi$ define a residual circulation, $\overline{X}$ is an external forcing, $\overline{(\cdot)}$ denotes a zonal average, and $\nabla\cdot\mathbf{F}$ is the divergence of the Eliassen–Palm flux. Its components are given by

$$F^{(\phi)} \equiv (\rho_0 a\cos\phi)(\overline{u}_z\overline{v'\theta'}/\overline{\theta}_z - \overline{v'u'}) \tag{4.2a}$$

$$F^{(z)} \equiv (\rho_0 a\cos\phi)\{[f - (a\cos\phi)^{-1}(\overline{u}\cos\phi)_\phi] \times \overline{v'\theta'}/\overline{\theta}_z - \overline{w'u'}\}, \tag{4.2b}$$

and the divergence is

$$\nabla\cdot\mathbf{F} = (a\cos\phi)^{-1}(F^{(\phi)}\cos\phi)_\phi + F^{(z)}_z.$$

The primed quantities represent the departure from a time- and zonally independent basic state. In the present work, the departure quantities have been defined with respect to a time mean state, but this state is sufficiently zonally symmetric to consider the previous equations to be relevant (this is especially true in the upper stratosphere and in the mesosphere, where the orographic effects are less prevailing).

In order to quantify the role of each mode on the zonal mean flow and on the residual circulation, the departure quantities in Eq. (4.2) have been replaced by a chosen mode (or a sum of chosen modes) obtained from the simplified analysis described earlier. The modes relate to their vertical velocity by projecting the departure from the time mean vertical velocity on the principal components:

$$w'_n(\mathbf{x}) = \frac{1}{2T}\int_{-T}^{T} a_n^*(t)w'(\mathbf{x}, t)\,dt. \quad (4.3)$$

The first-order eddy forcing of the TEM equations is given by the small-amplitude version of the Eliassen–Palm flux divergence, which is schematically written

$$\nabla\cdot\mathbf{F} = \nabla\cdot\left(\sum_{m,n} g_n\mathbf{G}g_m\right) = \sum_n \nabla\cdot g_n\mathbf{G}g_n + \nabla\cdot\left(\sum_{m,n(m\neq n)} g_n\mathbf{G}g_m\right), \quad (4.4)$$

where $g_n\mathbf{G}g_m$ denotes the quadratic form of the Eliassen–Palm flux. The last term on the right-hand side of Eq. (4.4) represents the cross terms and it vanishes when the flux divergence is time averaged, due to the orthogonality of the principal components. The time-averaged eddy forcing is thus the sum of the forcing produced by each mode, and it represents nonconservative and nonlinear effects since

$$\left\langle\frac{\partial\overline{J}}{\partial t}\right\rangle = 0 = -\langle\nabla\cdot\mathbf{F}\rangle + \langle\overline{S}\rangle + O(\alpha^3), \quad (4.5)$$

where $\langle\cdot\rangle$ denotes a time average, J is a wave activity, α is the amplitude of wave motion, and S represents an external forcing and nonconservative effects. Note that the nonacceleration theorem states that the divergence of the Eliassen–Palm flux vanishes for unforced linear waves, so they cannot transfer momentum to the mean state (Andrews et al. 1987). Under the assumption that our linear approximation is valid, the calculated budget of the Eliassen–Palm flux divergence can then locate the momentum sources and sinks of the flow under study.

We have calculated the time-averaged eddy forcing inside the three windows described earlier. Over the Rockies and the Pacific Ocean, it was also averaged over a latitude band ranging from 43° to 47°N. Over Central America, the zonal average was performed over a latitude band ranging from 8° to 12°N. Figure 16 shows the total eddy forcing at each location [in fact, the time average over five days of the right-hand side of Eq. (4.1) is plotted]. This was calculated from 262 to 0.07 hPa. Note that the plotted forcing is due solely to transient waves since exactly stationary waves are not described by these empirical modes. Over western North America (Fig. 16a), the eddy forcing is somewhat weak in the lower mesosphere (~ -7 m s^{-1} day^{-1}), and almost no eddy forcing is produced by propagating waves in the lower stratosphere. The most important contribution to the westward drag in the lower mesosphere near 0.3 hPa comes from the first few modes (with absolute period greater than ~40 h). Thus, this negative forcing could be created by large-scale mesospheric perturbations and quasi-stationary mountain waves that reached this level. Mode numbers greater than 20 (which correspond to an absolute period smaller than ~11 h) are almost exclusively tilting eastward (transporting positive momentum upward relative to the basic flow) and exert a positive forcing on the zonal flow near the 0.1-hPa level. If the eddy component of the flow consisted exclusively of a sum of modes ranging from 21 to 120 (representing one-third of the total variance), the forcing on the mean zonal flow would reach more than +5 m s^{-1} day^{-1} in the highest model levels, as is visible in Fig. 17a, showing that these modes are the major contributors to the mean flow acceleration at 0.1 hPa. These modes begin to dissipate (or are partly absorbed) just below the 1-hPa level. Figure 17b shows the eddy forcing produced by the modes ranging from 21 to 120 in the upper troposphere and lower stratosphere. The source of these waves is seen to be near the jet stream, as the negative value of -0.27 m s^{-1} day^{-1} indicates. This negative value suggests that waves transporting positive momentum relative to the mean flow are generated (since the production of waves with positive momentum should produce a negative forcing at the locus of emission, and a positive forcing somewhere else in the atmosphere, as is apparent in Fig. 17a). Unfortunately, the vertical velocity field below 321 hPa was not available to us, and it is impossible to evaluate the deepness of this tropospheric source. Figures 16a,b also indicate a negative eddy forcing in the upper-tropospheric midlatitude region. This behavior has already been observed in the GFDL SKYHI model by Andrews et al. (1983) and is attributed to growing and decaying unstable baroclinic disturbances.

Over the midlatitude Pacific Ocean, the total eddy forcing exerted by propagating waves is almost everywhere positive (or zero) throughout the middle atmosphere, reaching a maximum of about 30 m s^{-1} day^{-1} at 0.5 hPa (~53 km). A small eddy forcing of about 10 m s^{-1} day^{-1} is also observed around 10 hPa (32 km) (see Fig. 16b). The time mean Rossby number was still relatively high (reaching maxima of the order of 0.5 to 0.8 in the oceanic jet stream) and inertia–gravity wave emission can be expected. However, the impact of these IGWs on the zonal mean flow and the residual circulation seems marginal since the time mean eddy forcing in the stratosphere and mesosphere is almost exclusively produced by the first two modes (with periods greater than ~40 h) and the contribution from the modes with higher frequencies is weak, as can be seen in Fig. 17c. This could be due to the presence of absorbing critical levels just above the jet stream that could partially inhibit upward inertia–gravity wave propagation, as discussed earlier in section 4b(2). Another possibility is that the inertia–gravity wave emission process generated westward- and eastward-propagating waves at an equal rate.

The eddy forcing over Central America around 10°N is negative almost throughout the model middle atmosphere (Fig. 16c) and it tends to drag the westerly mesospheric winds. This drag is essentially produced by

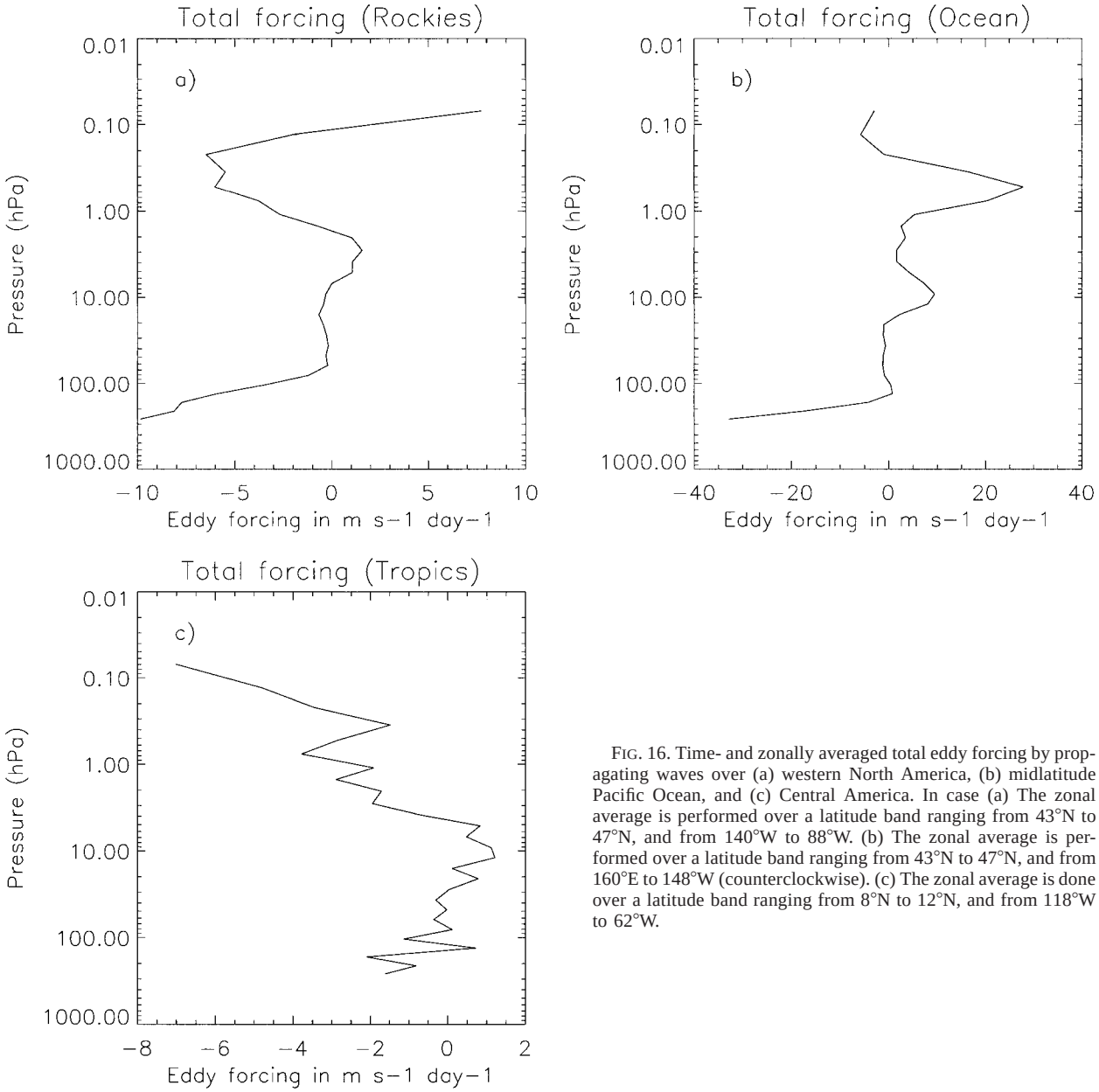

FIG. 16. Time- and zonally averaged total eddy forcing by propagating waves over (a) western North America, (b) midlatitude Pacific Ocean, and (c) Central America. In case (a) The zonal average is performed over a latitude band ranging from 43°N to 47°N, and from 140°W to 88°W. (b) The zonal average is performed over a latitude band ranging from 43°N to 47°N, and from 160°E to 148°W (counterclockwise). (c) The zonal average is done over a latitude band ranging from 8°N to 12°N, and from 118°W to 62°W.

westward-tilting inertia–gravity waves, and the main forcing comes from modes with absolute periods ranging from 4 to 13 h (see Figs. 16c, 17d). This means that the impact of propagating inertia–gravity waves on the mean flow was much more important over Central America than over the Pacific Ocean, as can be seen by comparing Figs. 17c and 17d. Figure 17c depicts the eddy forcing over the Pacific Ocean at midlatitudes produced by waves other than the first four modes (which describe large-scale structures), and this forcing is less than 1.5 m s^{-1} day^{-1}. In other words, inertia–gravity waves excited by the jet stream at midlatitudes have a weaker effect on the mean flow and the residual circulation than convectively generated inertia–gravity waves in the Tropics.

Note that these results seem different from the eddy forcing obtained in Hamilton et al. (1995). This is due to three main reasons: 1) nonpropagating waves are not included in our case, 2) a limited area is used, and 3) our time period (5 days) is shorter than what is used in Hamilton et al. (1995).

5. Summary and conclusions

In this paper, the theory of empirical normal modes of Brunet (1994) was adapted using pseudoenergy for

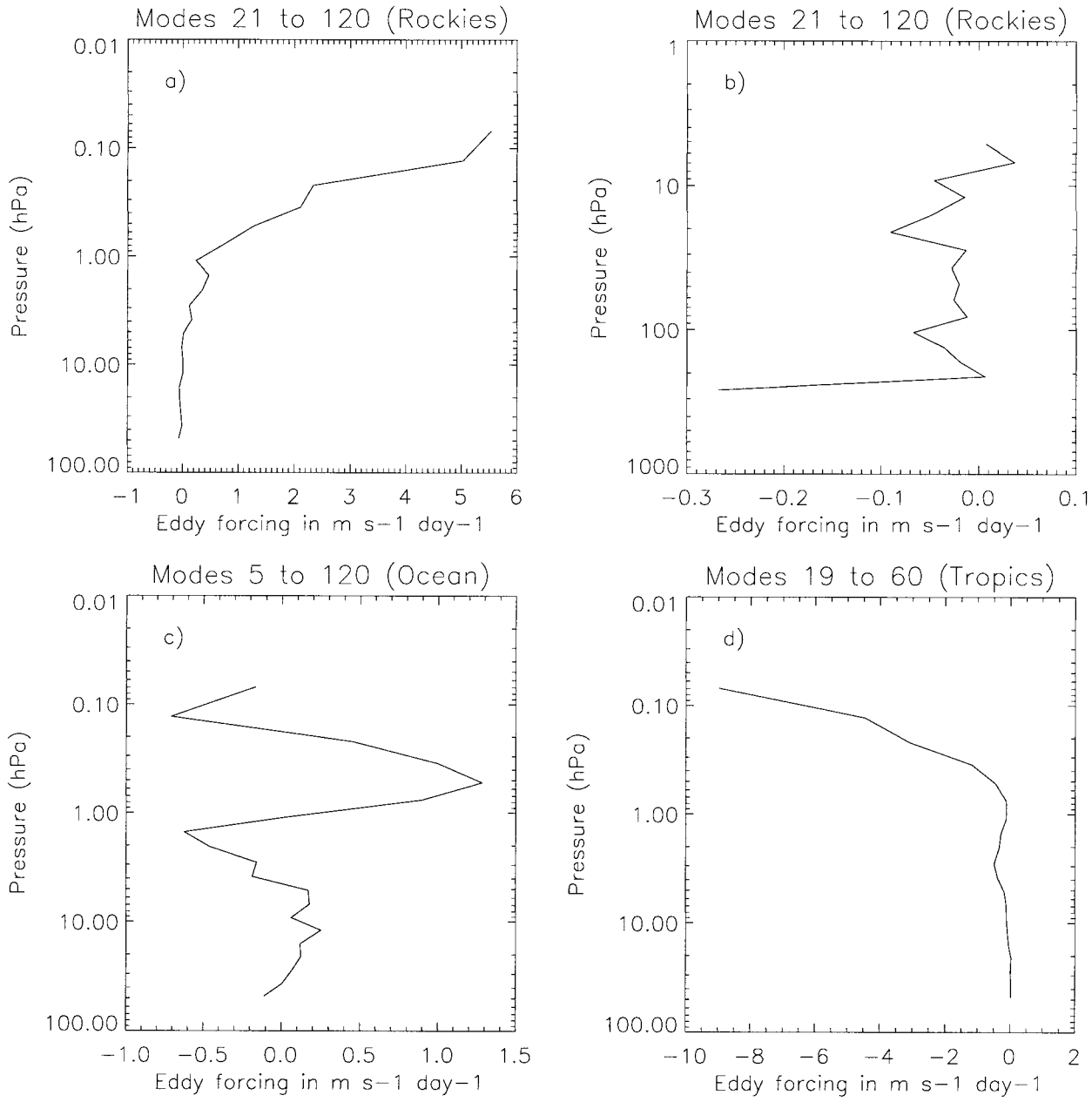

FIG. 17. Time- and zonally averaged eddy forcing by (a), and (b) modes with absolute period smaller than 11 h over western North America [(a) represents the forcing in the middle atmosphere, while (b) focuses on the upper troposphere and lower stratosphere; note the indication of the source region between 200 and 300 hPa]; (c) modes with absolute period smaller than 50 h over the Pacific Ocean; and (d) modes with absolute periods ranging from 4 to 13 h over Central America.

diagnosing atmospheric waves. An Eulerian approach based on the hydrostatic primitive equations in isentropic coordinates was described in order to extract monochromatic and dynamically balanced modes from atmospheric datasets. Moreover, it was shown that the presence of Rayleigh damping and Wiener forcing does not alter the empirical normal mode spatial structure, and that damping and noise are felt only through the broadening of the principal components. The approach was put into application by diagnosing relatively small-scale wave phenomena as simulated by the troposphere–stratosphere–mesosphere GFDL SKYHI model.

Three specific locations (the Rocky Mountain area, the midlatitude Pacific Ocean, and tropical Central America) were analyzed using a simplified version of

the theory. The simplification consists of using the wave energy instead of the pseudoenergy. Despite this simplification, which neglects shear processes in establishing the matrix **B**, quasi-monochromatic modes with some amplitude modulation were extracted from the dataset. The only empirical normal modes that could not be clearly classified as quasi-monochromatic in this study were the 20 leading mesospheric modes. The small-scale wave phenomena ($\sim$1000 km or less) had a narrow bandwidth (although with some amplitude modulation).

Over the Rockies, stationary mountain waves are dominant in the troposphere. In the lower stratosphere (200–20 hPa), stationary and propagating gravity waves are of the same order of magnitude, the propagating component being probably in large part due to time variation of the wind near the surface. The mesospheric gravity wave field is largely dominated by propagating inertia–gravity waves arising from the 200-hPa level, or lower. Jet stream excitation is thought to play a significant role in the inertia–gravity wave generation at midlatitudes since the time mean Rossby number can reach values of 0.5 to 0.6 on the upper and lower flank of the jet stream. The Eliassen–Palm flux divergence shows that propagating waves tend to exert a positive drag of $\sim$8 m s^{-1} day^{-1} on the highest model levels (at around 0.1 hPa and higher), while a negative drag of ~ -7 m s^{-1} day^{-1} is felt in the lower part of the mesosphere. The high- (low-) frequency component of the mesospheric flow with absolute period of about 10 h and lower (higher) exert the positive (negative) drag of 5 (-7) m s^{-1} day^{-1} around 0.07 hPa (0.3 hPa).

Over the midlatitude Pacific Ocean, inertia–gravity waves were observed in the model boundary layer. These waves were mostly absorbed between 800 and 600 hPa at Jones' critical levels. In the model middle atmosphere over this oceanic region, the inertia–gravity wave field had a very weak impact on the zonal mean flow and residual circulation and the Eliassen–Palm flux divergence was essentially due to the large-scale flow. A positive drag of 30 m s^{-1} day^{-1} was calculated in the lower part of the mesosphere. The mean Rossby number just above and below the jet stream was near unity at some locations, and jet stream IGW excitation was expected to occur.

Of the three analyzed regions, Central America was the only one where the inertia–gravity wave field (excluding IGWs excited by orography) exerted a negative drag on the zonally averaged zonal momentum equation. A drag of ~ -9 m s^{-1} day^{-1} in the mesosphere was mainly produced by waves with absolute periods smaller than 12 h.

Acknowledgments. We thank John Wilson (GFDL) for his help in providing the data from the GFDL SKYHI model. We also want to express our gratitude to Dinh Tran (McGill) for pointing out an error in an early version of this work, Peter Bartello (RPN), three anonymous reviewers for comments that led to improvements of the manuscript, and Bernard Dugas (RPN) for his technical assistance. Part of this work was done while one of us (MC) was visiting the Geophysical Fluid Dynamics Laboratory (NOAA/GFDL) in Princeton (New Jersey) during the summer of 1996 under a fellowship provided by Fonds pour la Formation de Chercheurs et Paide à la Recherche (FCAR). Martin Charron thanks Kevin Hamilton for his hospitality.

APPENDIX

Pseudoenergy in Pressure Coordinates

In pressure coordinates, the perturbation fields are defined relative to a basic state that is explicitly dependent on pressure. This means that the terms in the definition of the pseudoenergy appearing in Eq. (2.14) must be transformed according to

$$u' \rightarrow u' - \theta' u_{0p}/\theta_{0p} \tag{A.1a}$$

$$u_0 \rightarrow u_0 \tag{A.1b}$$

$$v' \rightarrow v' - \theta' v_{0p}/\theta_{0p} \tag{A.1c}$$

$$v_0 \rightarrow v_0 \tag{A.1d}$$

$$\sigma' \rightarrow \frac{1}{g\theta_{0p}} \frac{\partial}{\partial p}\left(\frac{\theta'}{\theta_{0p}}\right) \tag{A.1e}$$

$$\sigma_0 \rightarrow -(g\theta_{0p})^{-1} \tag{A.1f}$$

$$P' \rightarrow P' - \theta' P_{0p}/\theta_{0p} \tag{A.1g}$$

$$p' \rightarrow -\theta'/\theta_{0p} \tag{A.1h}$$

$$p_0 \rightarrow p_r\left(\frac{T_0}{\theta_0}\right)^{1/\kappa} \tag{A.1i}$$

$$\frac{\partial P_0}{\partial \phi} \rightarrow \frac{\partial P_0}{\partial \phi} - \left(\frac{\theta_{0\phi}}{\theta_{0p}}\right)\frac{\partial P_0}{\partial p}. \tag{A.1j}$$

Note that

$$\frac{d\psi_0}{dP_0} = -\frac{au_0\sigma_0}{\partial P_0/\partial \phi} = \frac{av_0\sigma_0 \cos\phi}{\partial P_0/\partial \lambda},$$

so every term in the definition of the pseudoenergy in isentropic coordinates has an equivalent in pressure coordinates. The Ertel potential vorticity P is given in pressure coordinates by

$$P = -g\theta_p\left[f - \frac{(u\cos\phi)_\phi}{a\cos\phi} + \frac{v_\lambda}{a\cos\phi}\right] + \frac{g\theta_\lambda v_p}{a\cos\phi} - \frac{g\theta_\phi u_p}{a}, \tag{A.2}$$

and this expression must be used in the right-hand side of (A.1). A volume element in θ coordinates, $a^2\cos\phi\, d\phi\, d\lambda\, d\theta$, becomes in pressure coordinates $a^2\,\theta_{0p}\cos\phi$

$d\phi\ d\lambda\ dp$. The bilinear form of the pseudoenergy $\mathbf{B}$ defined in Eq. (2.20) and the wave vector defined by Eq. (2.19) must be modified according to the correspondences of Eq. (A.1) and the new volume element. If the integrated pseudoenergy is written

$$\int a^2 \cos\phi\ d\phi\ d\lambda\ d\theta A = -\int g^{-1} a^2 \cos\phi\ d\phi\ d\lambda\ dp A_{(p)}, \qquad \text{(A.3)}$$

the bilinear form $\mathbf{B}_{(p)}$ and the wave vector $\mathbf{f}'_{(p)}$ become

$$\mathbf{B}_{(p)} = \begin{pmatrix} \frac{1}{2} & 0 & -\frac{u_0}{2} & 0 & b_{15} \\ 0 & \frac{1}{2} & -\frac{v_0}{2} & 0 & b_{25} \\ -\frac{u_0}{2} & -\frac{v_0}{2} & 0 & 0 & b_{35} \\ 0 & 0 & 0 & b_{44} & b_{45} \\ b_{51} & b_{52} & b_{53} & b_{54} & b_{55} \end{pmatrix}, \qquad \text{(A.4)}$$

where

$$b_{15} = b_{51} = -u_{0p}/(2\theta_{0p}) \qquad \text{(A.5a)}$$

$$b_{25} = b_{52} = -v_{0p}/(2\theta_{0p}) \qquad \text{(A.5b)}$$

$$b_{35} = b_{53} = (u_0 u_{0p} + v_0 v_{0p})/(2\theta_{0p}) \qquad \text{(A.5c)}$$

$$b_{45} = b_{54} = -a u_0 P_{0p} (2g\theta_{0p}^2)^{-1} (P_{0\phi} - \theta_{0\phi} P_{0p}/\theta_{0p})^{-1} \qquad \text{(A.5d)}$$

$$b_{44} = a u_0 (2g\theta_{0p})^{-1} (P_{0\phi} - \theta_{0\phi} P_{0p}/\theta_{0p})^{-1} \qquad \text{(A.5e)}$$

$$b_{55} = -\frac{\kappa c_p}{2p_r\theta_{0p}} \left(\frac{T_0}{\theta_0}\right)^{(\kappa-1)/\kappa} + \frac{u_{0p}^2 + v_{0p}^2}{2\theta_{0p}^2} + a u_0 P_{0p}^2 (2g\theta_{0p}^3)^{-1} (P_{0\phi} - \theta_{0\phi} P_{0p}/\theta_{0p})^{-1} \qquad \text{(A.5f)}$$

and

$$\mathbf{f}'_{(p)} = \begin{pmatrix} u' \\ v' \\ \frac{\partial}{\partial p}\left(\frac{\theta'}{\theta_{0p}}\right) \\ P' \\ \theta' \end{pmatrix}. \qquad \text{(A.6)}$$

Again, we use a five-dimensional wave vector in order to avoid the presence of differential operators in $\mathbf{B}_{(p)}$.

REFERENCES

Andrews, D. G., 1987: On the interpretation of the Eliassen–Palm flux divergence. *Quart. J. Roy. Meteor. Soc.*, **113,** 323–338.

——, J. D. Mahlman, and R. W. Sinclair, 1983: Eliassen-Palm diagnostics of wave–mean flow interaction in the GFDL ''SKYHI'' general circulation model. *J. Atmos. Sci.*, **40,** 2768–2784.

——, J. R. Holton, and C. B. Leovy, 1987: *Middle Atmosphere Dynamics*. Academic Press, 489 pp.

Bartello, P., 1995: Geostrophic adjustment and inverse cascades in rotating stratified turbulence. *J. Atmos. Sci.*, **52,** 4410–4428.

Breuer, K. S., and L. Sirovitch, 1991: The use of the Kharhunen-Loève procedure for the calculation of linear eigenfunctions. *J. Comput. Phys.*, **96,** 277–296.

Brunet, G., 1994: Empirical normal mode analysis of atmospheric data. *J. Atmos. Sci.*, **51,** 932–952.

——, and R. Vautard, 1996: Empirical normal modes versus empirical orthogonal functions for statistical prediction. *J. Atmos. Sci.*, **53,** 3468–3489.

Charney, J. G., and P. G. Drazin, 1961: Propagation of planetary-scale disturbances from the lower into the upper atmosphere. *J. Geophys. Res.*, **66,** 83–109.

Charron, M., 1998: Gravity wave diagnosis using empirical normal modes. Ph.D. thesis, McGill University, 128 pp. [Available from Department of Atmospheric and Oceanic Sciences, McGill University, 805 Sherbrooke Street West, Montréal, PQ H3A 2K6 Canada.]

Clark, T. L., T. Hauf, and J. P. Kuettner, 1986: Convectively forced internal gravity waves: Results from two-dimensional numerical experiments. *Quart. J. Roy. Meteor. Soc.*, **112,** 899–925.

Davis, P. A., and W. R. Peltier, 1979: Some characteristics of the Kelvin-Helmholtz and resonant overreflection modes of shear flow instability and of their interaction through vortex pairing. *J. Atmos. Sci.*, **36,** 2394–2412.

Fels, S. B., J. D. Mahlman, M. D. Schwarzkopf, and R. W. Sinclair, 1980: Stratospheric sensitivity to perturbations in ozone and carbone dioxide: Radiative and dynamical responses. *J. Atmos. Sci.*, **37,** 2265–2297.

Fritts, D. C., 1982: Shear excitation of atmospheric gravity waves. *J. Atmos. Sci.*, **39,** 1936–1952.

——, 1984: Shear excitation of atmospheric gravity waves. Part II: Nonlinear radiation from a free shear layer. *J. Atmos. Sci.*, **41,** 524–537.

——, and Z. Luo, 1992: Gravity wave excitation by geostrophic adjustment of the jet stream. Part I: Two-dimensional forcing. *J. Atmos. Sci.*, **49,** 681–697.

Grimshaw, R., 1975: Internal gravity waves: Critical layer absorption in a rotating fluid. *J. Fluid Mech.*, **70,** 287–304.

Hamilton, K., 1995: Comprehensive simulation of the middle atmosphere climate: Some recent results. *Climate Dyn.*, **11,** 223–241.

——, R. J. Wilson, J. D. Mahlman, and L. J. Umscheid, 1995: Climatology of the SKYHI troposphere–stratosphere–mesosphere general circulation model. *J. Atmos. Sci.*, **52,** 5–43.

Hayashi, Y., 1982: Space-time spectral analysis and its applications to atmospheric waves. *J. Meteor. Soc. Japan,* **60,** 156–171.

——, D. G. Golder, J. D. Mahlman, and S. Miyahara, 1989: The effect of horizontal resolution on gravity waves simulated by the GFDL ''SKYHI'' general circulation model. *Pure Appl. Geophys.*, **130,** 421–443.

Haynes, P. H., 1988: Forced, dissipative generalizations of finite-amplitude wave-activity conservation relations for zonal and nonzonal basic flows. *J. Atmos. Sci.*, **45,** 2352–2362.

Held, I. M., 1985: Pseudomomentum and the orthogonality of modes in shear flows. *J. Atmos. Sci.*, **42,** 2280–2288.

Hirota, I., and T. Hirooka, 1984: Normal mode Rossby waves observed in the upper stratosphere. Part I: First symmetric modes of zonal wavenumbers 1 and 2. *J. Atmos. Sci.*, **41,** 1253–1267.

Jones, W. L., 1967: Propagation of internal gravity waves in fluids with shear flow and rotation. *J. Fluid Mech.*, **30,** 439–448.

Lorenz, E. N., 1955: Available potential energy and the maintenance of the general circulation. *Tellus,* **7,** 157–167.

Lott, F., and H. Teitelbaum, 1993: Linear unsteady mountain waves. *Tellus,* **45A,** 201–220.

Luo, Z., and D. C. Fritts, 1993: Gravity-wave excitation by geo-

strophic adjustment of the jet stream. Part II: Three-dimensional forcing. *J. Atmos. Sci.,* **50,** 104–115.

Mahlman, J. D., and L. J. Umscheid, 1984: Dynamics of the middle atmosphere: Successes and problems of the GFDL ''SKYHI'' general circulation model. *Dynamics of the Middle Atmosphere,* J. R. Holton and T. Matsuno, Eds., Terrapub, 501–525.

Miyahara, S., Y. Hayashi, and J. D. Mahlman, 1986: Interactions between gravity waves and planetary-scale flow simulated by the GFDL ''SKYHI'' general circulation model. *J. Atmos. Sci.,* **43,** 1844–1861.

O'Sullivan, D., and T. J. Dunkerton, 1995: Generation of inertia–gravity waves in a simulated life cycle of baroclinic instability. *J. Atmos. Sci.,* **52,** 3695–3716.

Preisendorfer, R. W., 1988: *Principal Component Analysis in Meteorology and Oceanography*. Elsevier, 425 pp.

Sirovitch, L., and R. Everson, 1992: Management and analysis of large scientific datasets. *Int. J. Supercomput. Applic.,* **6,** 50–68.

Sutherland, B. R., and W. R. Peltier, 1995: Internal gravity wave emission into the middle atmosphere from a model tropospheric jet. *J. Atmos. Sci.,* **52,** 3214–3235.

——, C. P. Caulfield, and W. R. Peltier, 1994: Internal gravity wave generation and hydrodynamic instability. *J. Atmos. Sci.,* **51,** 3261–3280.

Wurtele, M. G., A. Datta, and R. D. Sharman, 1996: The propagation of gravity-inertia waves and lee waves under a critical level. *J. Atmos. Sci.,* **53,** 1505–1523.